CENTRO DE INVESTIGACIONES
EN ÓPTICA, A.C.

SPATIALLY RESOLVED POLARIMETRY USING CONVENTIONAL AND UNCONVENTIONAL POLARIZATION STATES

Dr. Sc. Thesis

Doctorado en Ciencias (Óptica)

Student: M.O. Guadalupe López Morales

Adviser: Dr. Rafael Espinosa Luna

February 23, 2017

León, Guanajuato, México

ABSTRACT

In this thesis work, some applications of the polarimetry techniques using conventional and unconventional polarized incident light are presented. The first part of this work consists on the study of the polarization properties of light scattered by a metallic cylinder. The angularly resolved Mueller matrix is determined experimentally as well as its main polarimetric parameters, which confirm that depolarization effects are not present. To our knowledge, this is the cheapest and easiest way to generate uniform horizontal and vertical linear polarizations scattered angularly. In the second part, the refractive index of a dielectric sample using highly focused radially polarized light is estimated by means of the measured Brewster's angle (according to the comments of the Reviewer of the generated article, this contribution represents a novel, reliable, and simple method). The Brewster's angle was determined by analyzing the images reflected by the sample in the optical field at the pupil plane of a high numerical aperture objective lens. Employing a high numerical-aperture objective lens allows the measurement of multiple angles of incidence from 0° to 64°, around a full circle, in a single shot. The theoretical and experimental results were compared, obtaining a remarkable consistency.

RESUMEN

En este trabajo de tesis se presentan algunas aplicaciones de las técnicas polarimétricas usando luz incidente polarizada convencional y no-convencionalmente. La primera parte de este trabajo consiste en el estudio de las propiedades de polarización de la luz dispersada por un cilindro metálico mediante la determinación experimental de la matriz de Mueller resuelta angularmente, así como de sus principales parámetros polarimétricos que confirman que no hay efectos de despolarización. A nuestro entender, ésta es la manera más fácil y de bajo costo de generar polarizaciones lineales horizontales y verticales uniformes dispersadas angularmente. En la segunda parte, se calcula la medida del índice de refracción de una muestra dieléctrica utilizando luz radialmente polarizada mediante la determinación experimental del ángulo de Brewster (de acuerdo a los comentarios de los Revisores del artículo generado, ésta contribución representa un método novedoso, confiable y sencillo). El ángulo de Brewster fue determinado a través del análisis de la imagen reflejada por la muestra en el plano de la pupila de una lente objetivo de alta apertura numérica. El empleo de una lente objetivo de alta apertura numérica permite medir múltiples ángulos de incidencia de 0 ° a 64 °, alrededor de un círculo, en un solo disparo. Se compararon los resultados teóricos y experimentales, obteniéndose una marcada consistencia.

DEDICATION

I dedicate this triumph to my sweet and loving parents, José Ángel and María Elena, who provided me their love and support necessary at all times to overcome any adversity.

This success in my life is dedicated to them with all my love…

Lupita.

ACKNOWLEDGEMENTS

Foremost, I am highly grateful to God for giving me the gifts of wisdom and understanding to finish this research work. Thank you for giving me the courage to go ahead and fulfill my dreams.

To my family and friends for taking me into account in their prayers, for their unconditional support, and because I have always had their confidence and love.

To all those people who have appeared unexpectedly in my path and who have left an indelible mark on my life. Thank you for your advice, for listening to me, for being there when I have to make important decisions, for sharing a little of your lives with me and for brightening my day with your presence.

To the Optical Research Center (CIO, Centro de Investigaciones en Óptica, A. C.) for allowing me to use their facilities and equipment to carry out my thesis. I am grateful to the CIO researchers for the academic and personal training I received during my doctoral formation. Special thanks to Dr. Rafael Espinosa Luna, my thesis advisor, for his full support in the realization of this thesis and for being my guide during my doctoral formation as a researcher. Thank you for giving me your valuable contributions, constant dedication and confidence, and for teaching me that there is not only knowledge, but also there are bonds of friendship and people of great human quality. I am grateful to the Synods who enriched the content of this thesis with their comments and observations. I also thank for his unselfish collaboration in my researching to Prof, Qiwen Zhan, Mc. Izcoatl Saucedo, MS. Victor Rico, MS. Yuliana Espinosa, and to the optical and mechanical workshop technicians.

Finally, I thank CONACYT for granting me a scholarship to carry out my doctoral studies.

Index

Chapter 1 Introduction

Polarization is a branch of optics that studies the behavior of the light and its interaction with the matter, thus it has found potential applications in several research areas like the optical characterization of materials, microscopy, biomedical applications, remote sensing, optical fibers, holography, among many others [1-7]. For many years, the light has been considered as an optical beam with spatially homogeneous polarization states, such as linear, circular, and elliptical conventional polarization states [8]. The recent advances in high-power computing and micro- and nano-fabrication techniques have allowed to the generating of unconventional light polarization states, namely optical beams with spatially variant states of polarization within the beam cross-section [9].

In this thesis work, conventional and unconventional polarization states were used to study the polarimetric behavior of light when interacting with certain materials. Applying conventional polarization states, the polarization properties of light scattered by a metallic cylinder were obtained through the analysis of its experimental angularly resolved Mueller matrix. On the other hand, a polarimetric arrangement was developed using a high numerical aperture microscope objective lens in order to determine the refractive index of a dielectric sample, using conventional and unconventional polarization states as the illumination source. This technique was proposed by the Prof. Qiwen Zhan during my predoctoral stay at the University of Dayton in Dayton, Ohio, USA, which was complemented by my advisor, Dr. Rafael Espinosa Luna, who proposed me to use unconventional polarization as the illumination source.

The fundamental concepts of the polarized light and polarimetry are presented in Chapter 2. The basic principles of the light reflection and transmission, including the Snell's law and Fresnel's equations, are introduced in this section in order to understand how the Brewster's angle and the refractive index are determined. In addition, the definition of the conventional polarization states and their linear interaction with optical media through the Mueller and the Jones formalism are explained. Because the polarimetry involves the measurement of the state of polarization of the light, some polarimeter arrangements and their applications are mentioned briefly. By last, the unconventional polarization is defined as well as some techniques to generate their most representative polarization states: radial and azimuthal.

In Chapter 3, the experimental methodology, results, and discussions of this work are presented. This chapter consists of two sections. In the first, the experimental determination of the angularly resolved Mueller matrix and its main polarimetric properties associated to light scattered by a metallic cylinder are discussed. In the second part, the methodology and results obtained through the experimental measurement of the Brewster's angle are discussed as a novel, reliable, and simple method for the determination of the refractive index of a dielectric sample. A particular importance is associated to the use of the radial polarization as an unconventional incident polarization state capable of providing information related to the homogeneous and isotropic character of the samples under study.

The General Conclusions and the Work at Future of this thesis work are contained in the Chapters 4 and 5, respectively. The final part of this thesis, the Appendix section, includes the Matlab codes used to obtain the simulated results as well as for the handling of the data obtained by the experimental results.

Papers published

The papers generated during the four years of my doctoral formation as a researcher are enlisted following lines:

1. **Guadalupe López-Morales**, Rafael Espinosa-Luna, and Claudio Frausto-Reyes "*Optical characterization of amber from Chiapas, Mexico*", *Proc. SPIE* 8873, Polarization Science and Remote Sensing VI, 887311 (2013).

2. **G. López-Morales**, R. Espinosa-Luna and C. Frausto-Reyes, *Optical characterization of amber from Chiapas*, Rev. Mex. Fís. **60**(3), 217–221 (2014).
3. I. Saucedo-Orozco, **G. López-Morales**, and R. Espinosa-Luna, "Generation of unconventional polarization from light scattered by metallic cylinders under conical incidence," Optics Letters **39**(18), 5341-5344 (2014).
4. **Guadalupe Lopez-Morales**, Victor-Manuel Rico-Botero, Rafael Espinosa-Luna, and Qiwen Zhan, "Refractive index measurement of dielectric samples using highly focused radial polarized light (Invited Paper)," Chin. Opt. Lett. **15**(3), 030004 (2017).
5. R. Espinosa-Luna, **G. Lopez-Morales**, V. M. Rico-Botero, E. Aguilar-Fernández, "Spatial average symmetry associated to unconventional polarization," Rev. Mex. Fis. **63**(2), 205-210 (2017).
6. **Guadalupe Lopez-Morales**, Izcoatl Saucedo-Orozco, Rafael Espinosa-Luna, Qiwen Zhan, Francisco Villa-Villa, "Polarization properties of light scattered by a metallic cylinder," (Manuscript in revision) Rev. Mex. Fís. (2017).

Conferences and workshops

- **Guadalupe López Morales**, Rafael Espinosa-Luna, Claudio Frausto Reyes, "Estudio de la degradación del ámbar de Chiapas mediante espectroscopia Raman," X Encuentro Participación de la Mujer en la Ciencia, León, Guanajuato (2013).

- **Guadalupe López-Morales**, Rafael Espinosa-Luna, and Claudio Frausto-Reyes, "Optical characterization of amber from Chiapas, Mexico," SPIE Optics + Photonics International Congress, San Diego, California, USA (2013).

- **Guadalupe López-Morales**, Rafael Espinosa-Luna, Claudio Frausto-Reyes, and Gil Arturo Pérez-Herrera, "Study of the degradation of amber from México by Raman spectroscopy," Mexican Optics and Photonics Meeting (MOPM) Ensenada, Baja California (2013).

- **Guadalupe López-Morales**, Izcoatl Saucedo-Orozco, Rafael Espinosa-Luna, and Qiwen Zhan, “Polarization properties of light scattered by a metallic cylinder,” Mexican Optics and Photonics Meeting (MOPM). León, Guanajuato (2015).

- **Guadalupe López-Morales**, Víctor-Manuel Rico-Botero, Rafael Espinosa-Luna, Qiwen Zhan, “Microellipsometry with unconventional polarization,” XXV International Material Research Congress, Cancún, Q. Roo, México (2016).

- **Guadalupe López-Morales**, Rafael Espinosa-Luna, Victor-Manuel Rico-Botero, Eusebio Aguilar-Fernández, “Spatial Average Stokes vector for unconventional polarizations,” LIX Congreso Nacional de Física, León, Guanajuato (2016).

- Workshop entitled “Ellipsometry School” at Instituto de Investigaciones en Comunicación Óptica, Universidad Autónoma de San Luis Potosí (2015).

- Oral talk entitled “Aplicaciones de la Microelipsometría” at Instituto Tecnológico de Tuxtla Gutiérrez, Chiapas (2016).

Chapter 2 Polarized light and polarimetry

Polarization is a phenomenon associated to the intrinsic vectorial, transversal nature of light. As one of the main branches of the Optics, it deals with the changes in the polarization state under propagation and its interaction with material media. Ordinary light emitted from the Sun or from a light bulb is named unpolarized, which means there does not exist a deterministic behavior of the orientation of its electric or magnetic fields with respect to its propagation direction. In this sense, there exist in Nature four main methods to obtain linear polarized light from unpolarized light; in other words, there exist four natural mechanisms, which convert unpolarized to linear polarized light (some insects also present the possibility to convert unpolarized to circularly polarized light). Polarization by transmission is generated by using a tourmaline gemstone, which acts like a dichroic filter and is made of a special material that transmits selectively a perpendicular component of the electric field along the certain direction (transmission axis), blocking the remaining polarization planes. Polarization by reflection occurs when the unpolarized light is reflected between two transparent media and the reflected light is partially polarized. On the other hand, some transparent crystals, such as calcite and quartz, have the optical property to split the refracted beam into two rays that are polarized in mutually perpendicular directions. These kinds of materials can polarize the light by refraction. The last method to polarize the light is by scattering, in which the unpolarized incident beam strikes to small particles or molecules of a material and scatters linearly polarized light in the plane perpendicular to the incident light; this effect contributes to the blueness of the sky.

The development of the polarimetry techniques has allowed understanding the relationship between polarimetric and physical properties of the matter through the study of the interaction of light with the material. The polarimetry has found fundamental and practical applications almost in every branch of science and technology.

2.1 Reflection and transmission of light

Light can be described as a transverse electromagnetic wave, which consists of an oscillating electric field $\vec{E}$ and an oscillating magnetic field $\vec{H}$ with the same frequency but oriented perpendicular to the wave-vector propagation direction [8, 10-11]. The Maxwell's equations for an isotropic non-conducting vacuum medium, without sources, are represented in the SI system by Eq. 2.1 [8,3]

$$\nabla\times\vec{E} = -\mu\frac{\partial\vec{H}}{\partial t}, \tag{2.1a}$$

$$\nabla\times\vec{H} = \varepsilon\frac{\partial\vec{E}}{\partial t}, \tag{2.1b}$$

$$\nabla\cdot\vec{E} = 0, \tag{2.1c}$$

$$\nabla\cdot\vec{H} = 0 \tag{2.1d}$$

where the constants μ and ε are the magnetic permeability and the permittivity of the media, respectively. ∇ is the nabla operator defined by $\nabla= \partial_x\hat{x} + \partial_y\hat{y} + \partial_z\vec{\hat{z}}$, where $\hat{x}, \hat{y}, \hat{z}$ represent the orthogonal unit vectors in the three-dimensional space.

The reflection and transmission of light are determined by the refractive index of the medium. Using Maxwell's equations (Eq. 2.1), the light behavior can be described through the well-known Fresnel's equations when it is reflected and transmitted at the plane or flat boundary between two different homogenous optically isotropic media [8].

The Fresnel's equations involve the amplitudes, phases, and polarizations of the reflected and transmitted light when the incident light passes through an interface between two transparent media with different indices of refraction. To calculated the Fresnel's equations it is necessary to use the Snell's law, which describes the bending of the path of the light when passing through the boundary between two isotropic media and is represented by Eq. 2.2 [8]

$$n_1 \sin\theta_i = n_2 \sin\theta_t, \tag{2.2}$$

where n_1 and n_2 are the refractive index of the incident and transmission media, respectively, and θ_i and θ_t are the incident and transmission angles, respectively (Fig.2.1).

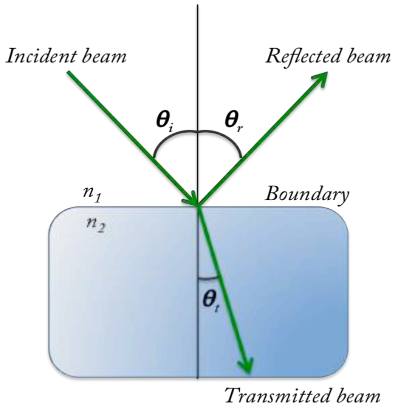

Fig. 2.1 Reflected and transmitted light at oblique incidence.

The reflected and transmitted light by a sample at oblique incidence can be studied for the two cases of the mutually orthogonal polarization states and both criteria are used to derivate the Fresnel's equations; the first case is when the electric field of the incident light is parallel to the incident plane (*p*-polarization) and the second case is when the incident light has its electric field perpendicular to the plane of incident (*s*-polarization). The relationships of the Fresnel's equations are represented by the Eq. 2.3 [8, 10-11]

$$r_p = -\frac{\tan(\theta_i - \theta_t)}{\tan(\theta_i + \theta_t)}, \tag{2.3a}$$

$$r_s = -\frac{\sin(\theta_i - \theta_t)}{\sin(\theta_i + \theta_t)}, \tag{2.3b}$$

$$t_p = \frac{2\cos\theta_i \sin\theta_t}{\sin(\theta_i + \theta_t)\cos(\theta_i - \theta_t)}, \tag{2.3c}$$

$$t_s = \frac{2\cos\theta_i \sin\theta_t}{\sin(\theta_i + \theta_t)}, \tag{2.3d}$$

where r_p and r_s are the coefficients of reflection, and t_p and t_s are the coefficients of transmission associated to the p- and s-polarization states, respectively. The reflected light can also be expressed in function of the incidence angle using the Snell's law (Eq. 2.2), as shown in the Eq. 2.4 [8, 10-11]

$$r_p = \frac{-n^2\cos\theta_i + \sqrt{n^2 - \sin^2\theta_i}}{n^2\cos\theta_i + \sqrt{n^2 - \sin^2\theta_i}}, \tag{2.4a}$$

$$r_s = \frac{\cos\theta_i - \sqrt{n^2 - \sin^2\theta_i}}{\cos\theta_i + \sqrt{n^2 - \sin^2\theta_i}}, \tag{2.4b}$$

where $n = \frac{n_2}{n_1}$.

The reflectance R is the ratio of the reflected light intensity I_r to incident light intensity I_i ($R = I_r/I_i$). The reflectances for p- and s-polarized light are expressed as Eq. 2.5 [8, 10-11]

$$R_p = \frac{I_{rp}}{I_{ip}} = \left|\frac{E_{rp}}{E_{ip}}\right|^2 = |r_p|^2, \tag{2.5a}$$

$$R_s = \frac{I_{rs}}{I_{is}} = \left|\frac{E_{rs}}{E_{is}}\right|^2 = |r_s|^2. \tag{2.5b}$$

2.1.1 The Brewster's angle

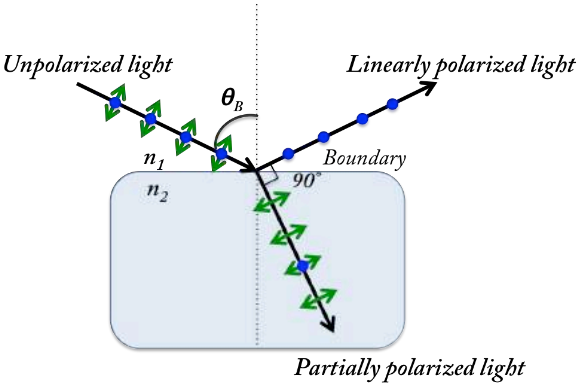

Fig. 2.2 Incident light at the Brewster's angle. The green arrows represent p-polarized light and the blue points represent s-polarized light.

If p-polarized light is incident upon a surface between two transparent media, the reflected electric field entirely disappears at a particular incident angle called the Brewster's angle, and the incident beam is totally transmitted into a second medium. From the Snell's law, the Brewster's angle θ_B is represented by the Eq. 2.6 and it is determined when the parallel reflection amplitude is zero and the incident and transmitted angles sum up to 90° [8, 10-11],

$$\theta_B = \tan^{-1}\left(\frac{n_2}{n_1}\right). \tag{2.6}$$

When unpolarized light strikes on a surface at the Brewster's angle, the reflected light is s-linearly polarized (perpendicular to the plane of incidence), and the transmitted light is partially polarized, as shows the Fig. 2.2.

2.1.2 Refractive index

The refraction of light is determined from the refractive index of the material that the incident light is going through and it is defined by Eq. 2.7 [8,11]

$$n = \frac{c}{v}, \tag{2.7}$$

where c is the speed of the light in the vacuum $(c = 2.99792 \times 10^8\ m/s)$ and v is the speed of light in the medium. In other words, the refractive index is the ratio of the speed of light to its speed in the medium.

It is important to mention there are media that show strong light absorption, and such a phenomenon cannot be expressed only with n. Thus, in order to describe light absorption by media, the extinction coefficient k is introduced and the Eq. 2.8 defines the complex refractive index N [8,11]

$$N = n + ik. \tag{2.8}$$

Most techniques used on the optical characterization require knowledge of the basic optical properties of the material under study. For that reason, several optical techniques to measure the refractive index are presented in Chapter 3.

2.2 Conventional polarization states and its linear interaction with optical media

Most sources of light in the Nature produce unpolarized or partially polarized light; it means that the direction of its electric field is completely or partially random. When the electric field of light waves is oriented along some specific direction, its associated state is referred to as polarized light; in this case, the polarization is conceptualized by superimposing the two mutually orthogonal components, and the phase difference between them has to be taken into account, in order to describe the state of polarization properly. According to this phase difference and the amplitudes of each component of the electric field, the state of polarization changes into various states ranging from linear to circular polarizations as particular states of the most general case, the elliptically polarized states.

2.2.1 Conventional polarization states

Conventional polarization states are based in the direction of the electric field oscillation and its spatial homogeneous distribution; in other words, the polarization state is (ideally) the same at any point of the illumination field. Linear and circular polarization states are normally used as conventional polarizations states.

From the Maxwell's equations (Eq. 2.1), the wave equation for the electric field component can be obtained using the Eq. 2.9 [8, 11]

$$\nabla^2\vec{E} = \frac{1}{\mu\varepsilon^2}\frac{\partial^2\vec{E}}{\partial t^2}. \tag{2.9}$$

Considering the rectangular Cartesian coordinate system as the reference system, the simplest solution to the wave equation is the electromagnetic plane wave that propagates in certain time t, along the z-direction, which can be described by the Eq. 2.10 [8]

$$\vec{E}(z,t) = \vec{E}_0\, exp[i(\omega t - Kz + \delta)], \tag{2.10}$$

where $\vec{E}_0$ is the electric field amplitude, ω is the angular frequency, $K = \frac{2\pi}{\lambda}$ the propagation number, δ is the spatial phase, and λ is the wavelength.

The plane electromagnetic wave is described by superimposing coherently two electric fields whose planes of oscillation are parallel to the x and y axes, respectively. The polarization state of light can be expressed as the vector sum of the electric fields $\vec{E}_x$ and $\vec{E}_y$, Eq. 2.11, and depends on the relative amplitude (E_{0x} and E_{0y}) and phase difference (δ_x and δ_y) of the two orthogonal components of the electric field, Eq. 2.12 [13]

$$\vec{E}(z,t) = \vec{E}_x(z,t) + \vec{E}_y(z,t), \tag{2.11}$$

$$\vec{E}(z,t) = \{E_{0x}\exp[i(\omega t - kz + \delta_x)]\}\vec{x} + \{E_{0y}\exp[i(\omega t - kz + \delta_y)]\}\vec{y}, \tag{2.12}$$

where $\vec{x}$ and $\vec{y}$ are unit vectors along the coordinate axes. To describe the state of polarization, the relative phase difference $\delta_y - \delta_x$ and also the direction at which the observer takes the register (looking to the source or to the propagation direction; in this thesis, the first criterion is assumed) are taken into account, as shown in Fig. 2.3. When $\delta_y - \delta_x = 0$ the polarization state is called linear polarization (Fig. 2.3a), there is no phase difference between $\vec{E}_x$ and $\vec{E}_y$. If the phase difference is 90° ($\delta_y - \delta_x = \pi/2$), and the amplitudes are equal, the polarization state is known as circular right-handed polarization (Fig. 2.3b). Fig. 2.3c is referred to as elliptical polarization when the amplitudes are different and $\delta_y - \delta_x = \pi/4$.

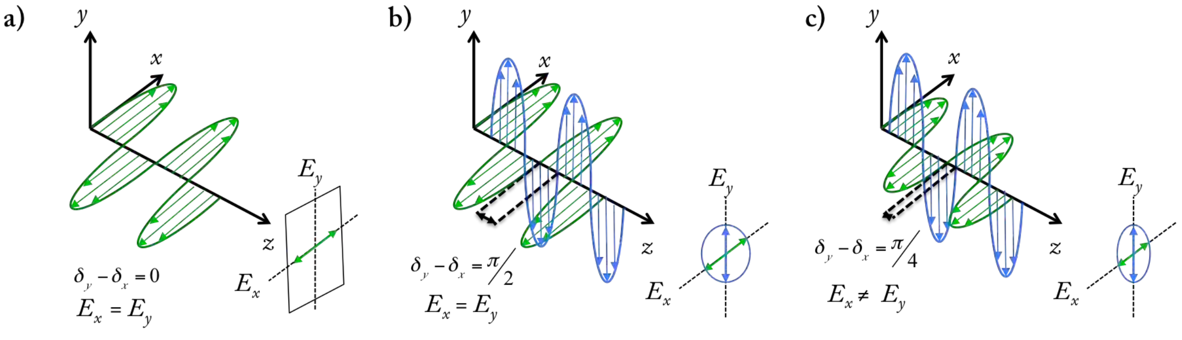

Fig. 2.3 Representations of (a) linear, (b) circular right-handed, and (c) elliptical polarization.

2.2.2 The Stokes polarization parameters

The Stokes parameters describe the polarization state of any incident beam through the light intensities and they were defined by George Gabriel Stokes in 1852 [12]. If in Eq. 2.12 the value for z is equal to zero, the electric fields E_x and E_y become as the Eqs. 2.13 and 2.14, respectively [12]

$$\vec{E}_x(t) = \vec{E}_{0x} \exp[i(\omega t + \delta_x)] = \vec{E}_x \exp(i\omega t), \tag{2.13}$$

$$\vec{E}_y(t) = \vec{E}_{0y} \exp\left[i\left(\omega t + \delta_y\right)\right] = \vec{E}_y \exp(i\omega t), \tag{2.14}$$

where

$$\vec{E}_x = \vec{E}_{0x} \exp(i\delta_x), \tag{2.15}$$

$$\vec{E}_y = \vec{E}_{0y} \exp\left(i\delta_y\right) \tag{2.16}$$

are complex amplitudes. The Stokes parameters (S_0, S_1, S_2, S_3) are represented in terms of the orthogonal component amplitudes (E_{0x} and E_{0y}) and their relative phase difference $\delta_y - \delta_x$. The Stokes parameters for a plane monochromatic wave are defined in complex notation by the following relationships, Eq. 2.17 [13-14]

$$S_0 = E_x E_x^* + E_y E_y^*, \tag{2.17a}$$

$$S_1 = E_x E_x^* - E_y E_y^*, \tag{2.17b}$$

$$S_2 = E_x E_y^* + E_y E_x^*, \tag{2.17c}$$

$$S_3 = i\left(E_x E_y^* - E_y E_x^*\right), \tag{2.17d}$$

where $i = \sqrt{-1}$ and the asterisk symbol (*) represents the operation of the conjugate complex. Substituting the Eqs. 2.15 and 2.16 into the previous equations (Eq. 2.17) gives [13-14]

$$S_0 = E_{0x}^2 + E_{0y}^2 \tag{2.18a}$$

$$S_1 = E_{0x}^2 - E_{0y}^2 \tag{2.18b}$$

$$S_2 = 2E_{0x}E_{0y}\cos\delta \tag{2.18c}$$

$$S_3 = 2E_{0x}E_{0y}\sin\delta \tag{2.18d}$$

where $\delta = \delta_y - \delta_x$.

Using the Eq. 2.18, the representations of the most common polarized light states are obtained as shown in Table I [12].

Table I. The six basic polarization states represented by the unnormalized Stokes parameters.

Linear horizontally polarized light (LH) $E_{0y} = 0$	**Linear vertically polarized light (LV)** $E_{0x} = 0$
$S_0 = E_{0x}^2$	$S_0 = E_{0y}^2$
$S_1 = E_{0x}^2$	$S_1 = -E_{0y}^2$
$S_2 = 0$	$S_2 = 0$
$S_3 = 0$	$S_3 = 0$

Linear $\pm 45°$ polarized light (L±) $E_{0x} = E_{0y} = E_0$ and $\delta = 0°\ (180°)$	**Circularly Right/Left polarized light (CR/CL)** $E_{0x} = E_{0y} = E_0$ and $\delta = \pm 90°$
$S_0 = 2E_0^2$	$S_0 = 2E_0^2$
$S_1 = 0$	$S_1 = 0$
$S_2 = \pm 2E_0^2$	$S_2 = 0$
$S_3 = 0$	$S_2 = \pm 2E_0^2$

The four Stokes parameters (Eq. 2.18) are contained into a 4 x 1 column matrix, called the Stokes vector S, and are expressed as in the Eq. 2.19 [15]

$$S = \begin{bmatrix} S_0 \\ S_1 \\ S_2 \\ S_3 \end{bmatrix} = \begin{bmatrix} I_x + I_y \\ I_x - I_y \\ I_{+45} - I_{-45} \\ I_r - I_l \end{bmatrix}, \tag{2.19}$$

where I_j denotes the intensity associated to the analyzed polarization states $(j = x, y, +45, -45, r, l)$ and x represents linear horizontal, y linear vertical, $+45$ linear, -45 linear, r circular right-, and l circular left-handed polarizations, respectively.

Therefore, the normalized Stokes vector for each state of polarization is shown in the Table II where I_0 is the total intensity and SOP represents the state of polarization [14].

Table II. The Stokes vector for each state of polarized light.

SOP	Stokes vector	SOP	Stokes vector
LH $E_{0y} = 0$ $I_0 = E_{0x}^2$	$S_x = I_0 \begin{bmatrix} 1 \\ 1 \\ 0 \\ 0 \end{bmatrix}$	LV $E_{0x} = 0$ $I_0 = E_{0y}^2$	$S_y = I_0 \begin{bmatrix} 1 \\ -1 \\ 0 \\ 0 \end{bmatrix}$
L+ $E_{0x} = E_{0y} = E_0$ $\delta = 0°$ $I_0 = 2E_0^2$	$S_+ = I_0 \begin{bmatrix} 1 \\ 0 \\ 1 \\ 0 \end{bmatrix}$	L− $E_{0x} = E_{0y} = E_0$ $\delta = 180°$ $I_0 = 2E_0^2$	$S_- = I_0 \begin{bmatrix} 1 \\ 0 \\ -1 \\ 0 \end{bmatrix}$
CR $E_{0x} = E_{0y} = E_0$ $\delta = +90°$ $I_0 = 2E_0^2$	$S_r = I_0 \begin{bmatrix} 1 \\ 0 \\ 0 \\ 1 \end{bmatrix}$	CL $E_{0x} = E_{0y} = E_0$ $\delta = -90°$ $I_0 = 2E_0^2$	$S_l = I_0 \begin{bmatrix} 1 \\ 0 \\ 0 \\ -1 \end{bmatrix}$

2.2.3 Mueller's matrix calculus

The Mueller's matrix (M) is a 4 x 4 matrix whose all elements are real and represent the linear response of the medium under study to the intensity associated to an incident beam. The Mueller's matrices can describe systems that depolarize or not depolarize, partially or fully the light, and provide the complete polarimetric description of the response of a medium to excitation by polarized light. The linear response of a physical system transforms the incident polarization state S^{inc} into the outgoing Stokes vector S^{out}, which is represented by the Eq. 2.20 and 2.21 [1, 14]

$$S^{out} = MS^{inc} \tag{2.20}$$

$$S^{out} = \begin{pmatrix} m_{00} & m_{01} & m_{02} & m_{03} \\ m_{10} & m_{11} & m_{12} & m_{13} \\ m_{20} & m_{21} & m_{22} & m_{23} \\ m_{30} & m_{31} & m_{32} & m_{33} \end{pmatrix} \begin{pmatrix} S_0^i \\ S_1^i \\ S_2^i \\ S_3^i \end{pmatrix} = \begin{pmatrix} S_0^o \\ S_1^o \\ S_2^o \\ S_3^o \end{pmatrix}. \tag{2.21}$$

The form of the M depends strongly on the morphological symmetries of the sample under study [16], but the Mueller parameter values depend on the nature of the sample. The M parameters have also been determined, independently of the dielectric properties of the one-dimensional (1D) surface and its depolarization properties, at the optical physical approximation limit [17-22]. A one-dimensional (1D) surface is a surface whose profile changes only along one direction, but it is kept constant along its perpendicular direction (a linear diffraction grating is a 1D surface) and has associated a Mueller's matrix with the form given by Eq. 2.22 [17]

$$M_{1D} = \begin{pmatrix} m_{00} & m_{01} & 0 & 0 \\ m_{01} & m_{00} & 0 & 0 \\ 0 & 0 & m_{22} & m_{23} \\ 0 & 0 & -m_{23} & m_{22} \end{pmatrix}. \tag{2.22}$$

Note that $m_{00} = m_{11}, m_{01} = m_{10}, m_{22} = m_{33}, m_{23} = -m_{32}$, and the elements $m_{02}, m_{03}, m_{12}, m_{13}, m_{20}, m_{21}, m_{30},\ m_{31}$ are zero. If the 1D surface does not depolarize the polarized incident light, then only three parameters are independent, because $m_{00}^2 = m_{01}^2 + m_{22}^2 + m_{23}^2$ [23]. Some systems as one-dimensional rough metallic surfaces [22], small homogeneous spheres [24], biological particles with spherical form [25], nano-imprinted grating structures [26], and thin film of silica (SiO2) thermally grown on a crystalline silicon (c-Si) wafer [27], are represented by the same matricial form as 1D surface.

2.2.3.1 Mueller's matrix of a linear polarizer

A linear polarizer is an optical element utilized to obtain linearly polarized light from unpolarized light; in other words, it attenuates one of the orthogonal components of an optical beam (as the tourmaline crystal or the commercial dichroic sheets). Considering a birefringent behavior, the two orthogonal transmission axes are designated p_x and p_y, perpendicular to the propagating direction [12, 14]. A polarizer used to produce polarized light is known as a generator, and if it is used to analyze polarized light, it is called an analyzer.

Taking into account that the components of the incident beam are represented by E_x and E_y, the outgoing beam from the polarizer has the components E'_x and E'_y, and they are parallel to the original axes of the birefringent medium. The Eq. 2.23 represents the emerged electric fields [12, 14]

$$E'_x = p_x E_x \qquad 0 \leq p_x \leq 1, \tag{2.23a}$$

$$E'_y = p_y E_y \qquad 0 \leq P_y \leq 1. \tag{2.23b}$$

The factors p_x and p_y are the amplitude attenuation coefficients along the orthogonal transmission axes. The Mueller's matrix for a polarizer is given by Eq. 2.24 [12, 14]

$$M = \frac{1}{2}\begin{pmatrix} p_x^2 + p_y^2 & p_x^2 - p_y^2 & 0 & 0 \\ p_x^2 - p_y^2 & p_x^2 + p_y^2 & 0 & 0 \\ 0 & 0 & 2p_x p_y & 0 \\ 0 & 0 & 0 & 2p_x p_y \end{pmatrix}. \tag{2.24}$$

When the axes of the polarizing components have been rotated through an angle θ with respect to the x' and y' axes, the Mueller's matrix for a rotated polarizer can be obtained using the Eq. 2.25 [12, 14]

$$M_{LP} = \frac{1}{2}\begin{pmatrix} 1 & \cos 2\gamma \cos 2\theta & \cos 2\gamma \sin 2\theta & 0 \\ \cos 2\gamma \cos 2\theta & \cos^2 2\theta + \sin 2\gamma \sin^2 2\theta & (1 - \sin 2\gamma) \sin 2\theta \cos 2\theta & 0 \\ \cos 2\gamma \sin 2\theta & (1 - \sin 2\gamma) \sin 2\theta \cos 2\theta & \sin^2 2\theta + \sin 2\gamma \cos^2 2\theta & 0 \\ 0 & 0 & 0 & \sin 2\gamma \end{pmatrix}, \quad \textbf{(2.25)}$$

where $0 \leq \gamma \leq 90°$. For a linear horizontal polarizer $\gamma = 0°$, and for a linear vertical polarizer $\gamma = 90°$. The physical rotation of θ leads to the appearance of 2θ in rather than θ because it is working in the intensity domain.

2.2.3.2 Mueller's matrix of a linear retarder

A retarder is an optical device used to transmit light while modifying its polarization state without attenuating, deviating, or displacing the beam, and also changes the phase of the optical beam. A retarder generates a phase difference (ϕ) between the orthogonal electric field vector components $\vec{E}_x$ and $\vec{E}_y$ of the incident beam. The Mueller's matrix for a retarder with a phase shift ϕ and fast axis along the x-axis, is given by Eq. 2.26 [12, 14]

$$M_R = \begin{pmatrix} 1 & 0 & 0 & 0 \\ 0 & 1 & 0 & 0 \\ 0 & 0 & \cos\phi & \sin\phi \\ 0 & 0 & -\sin\phi & \cos\phi \end{pmatrix} \quad \textbf{(2.26)}$$

When the phase of one component of the light is delayed with respect to the orthogonal component by a quarter wave, it means that $\phi = \pi/2$, the retarder is called a quarter-wave plate. It converts the linear polarization to circular polarization and vice-versa. For a half-wave plate, $\phi = \pi$, the phase of one component of the light is delayed with respect to the orthogonal component by a half wave.

The Mueller's matrix for the rotated retarder is given by Eq. 2.27 [12, 14]

$$M_{R(\phi,2\theta)} = \begin{pmatrix} 1 & 0 & 0 & 0 \\ 0 & \cos^2 2\theta + \cos\phi \sin^2 2\theta & (1 - \cos\phi) \sin 2\theta \cos 2\theta & -\sin\phi \sin 2\theta \\ 0 & (1 - \cos\phi) \sin 2\theta \cos 2\theta & \sin^2 2\theta + \cos\phi \cos^2 2\theta & \sin\phi \cos 2\theta \\ 0 & \sin\phi \sin 2\theta & -\sin\phi \cos 2\theta & \cos\phi \end{pmatrix}. \quad \textbf{(2.27)}$$

2.2.4 Polarimetric scalar metrics

The polarimetric scalar metrics are relationships obtained through the Mueller's matrix elements, and they are used to describe some specific linear response of the illuminated medium by polarized light.

The depolarization index, $\mathrm{DI(M)}$ is defined as the Eq. 2.28 [28],

$$0 \leq \mathrm{DI(M)} = \left\{\textstyle\sum_{\mathrm{j,k}=0}^{3} \mathrm{m}_{\mathrm{jk}}^{2} - \mathrm{m}_{00}^{2}\right\}^{1/2} / \sqrt{3}\mathrm{m}_{00} \leq 1. \tag{2.28}$$

It is interpreted as the depolarization average generated by the medium to the incident polarization. The depolarization index seems to depend only on the medium properties and not on the characteristics of the incident light. This is not really true because the M represents just the response to the incident polarization. Its physical limits are interpreted as follows: 0 means the system depolarizes totally the incident light, while 1 means the system does not depolarize at all. The intermediate values are interpreted as a partial depolarization generated on the outgoing light.

Furthermore, the degree of polarization $DoP(M,S)$ and its physical realizable limits are defined by Eq. 2.29 [12, 29]

$$0 \leq DoP(M,S) = \frac{\sqrt{\left(S_1^o\right)^2 + \left(S_2^o\right)^2 + \left(S_3^o\right)^2}}{S_0^o} = \frac{\left[\sum_{j=1}^{3}\left(m_{j0}S_0^i + m_{j1}S_1^i + m_{j2}S_2^i + m_{j3}S_3^i\right)^2\right]^{1/2}}{m_{00}S_0^i + m_{01}S_1^i + m_{02}S_2^i + m_{03}S_3^i} \leq 1. \tag{2.29}$$

DoP is a measure of the percentage of polarized light associated to a light beam. The DoP usually is measured directly from the Stokes vector emerging from the system under study and the measured value is associated to the outgoing light; however, it is inherently related to the optical response of the system. The value of $DoP = 1$ corresponds to completely polarized light, $DoP = 0$ corresponds to unpolarized light, and $0 < DoP < 1$ corresponds to partially polarized light.

Other useful auxiliary polarimetric parameters are the polarizance $P(M)$and the diattenuation $D(M)$parameters, which are defined by Eq. 2.30 and 2.31, respectively [29]

$$0 \leq P(M) = \frac{\sqrt{m_{10}^2 + m_{20}^2 + m_{30}^2}}{m_{00}} \leq 1, \tag{2.30}$$

$$0 \leq D(M) = \frac{\sqrt{m_{01}^2 + m_{02}^2 + m_{03}^2}}{m_{00}} \leq 1. \tag{2.31}$$

$P(M)$ is interpreted as the capability of a given system to polarize un-polarized incident light; a high value is associated to a highly efficient polarizer, but a lower value is associated to a low or null polarizer behavior. $D(M)$ describes the diattenuation given by the system and indicates the intensity variation when an incident polarized state is transmitted or reflected. The upper limit, 1, is associated to a totally diattenuating system, while the lower value, 0, means the system does not attenuate at all. A system with intermediate values within the interval (0,1) is interpreted as a partial diattenuator or polarizer, respectively.

The $Q(M)$ metrics is defined by Eq. 2.32 [30-32]. The bounds on the metric *Q(M)* are $0 \leq Q(M) \leq 3$. Where $Q(M) = 0$ for a totally depolarizing medium; $0 < Q(M) < 1$ is for a partially depolarizing medium; $1 \leq Q(M) < 3$ represents a partially depolarizing medium if, in addition, $0 < DI(M) < 1$, otherwise, represents a non-depolarizing diattenuating medium; $Q(M) = 3$ is associated to a non-depolarizing non-diattenuating medium, that is, a pure dephaser or retarder [33]

$$0 \leq Q(M) = \frac{\sum_{i=2,j=1}^{4} m_{ij}^2}{\sum_{j=1}^{4} m_{1j}^2} = \frac{3[DI(M)]^2 - [D(M)]^2}{1 + [D(M)]^2} \leq 3. \tag{2.32}$$

The theorem of Gil-Bernabeu or the trace condition is usually employed to test if the system can be described by a Jones matrix, which is the case if the Eq. 2.33 is fulfilled, and then the Mueller matrix is termed Mueller-Jones matrix [34]

$$Tr(M^T M) = 4m_{00}^2, \tag{2.33}$$

where Tr denotes the trace and T the matrix transpose operation. If the values of Eq. 2.33 are within $0 \leq Tr(M^T M)/4m_{00}^2 < 1$, it means the system depolarizes and, as a consequence, it can not be described by a Jones matrix; otherwise, if the Eq. 2.33 is fulfilled, it can be described by a Jones matrix. This criterion is valid for any passive optical system.

2.2.5 The Jones matrix calculus

The Jones calculus is used to describe the coherent superposition of polarized light, this is because it operates on amplitudes and phases rather than intensities of the electric field. The electric vector of a monochromatic light wave traveling along the z-axis can be decomposed into its x and y components as E_x and E_y, respectively, which are in general complex quantities with an amplitude and a phase [8, 12]. The Jones vector contains the complex components of the electric vector of light in the form as the Eq. 2.34

$$\vec{E}(z,t) = \begin{pmatrix} E_x \\ E_y \end{pmatrix}, \tag{2.34}$$

where

$$E_x = E_{0x} \exp(i\delta_x) = |E_x| \exp(i\delta_x), \tag{2.35a}$$

$$E_y = E_{0y} \exp(i\delta_y) = |E_y| \exp(i\delta_y). \tag{2.35b}$$

The total intensity I of the optical field is given by Eq. 2.36 [12]

$$I = I_x + I_y = E_{ox}^2 + E_{oy}^2 = |E_x|^2 + |E_y|^2 = E_x E_x^* + E_y E_y^*. \tag{2.36}$$

The intensity can be obtained by the matrix multiplication as is shown in the Eq. 2.37

$$I = \begin{pmatrix} E_x^* & E_y^* \end{pmatrix} \begin{pmatrix} E_x \\ E_y \end{pmatrix} . \tag{2.37}$$

The Jones vector is generally expressed by the normalized light intensity ($I = 1$). Thus, the Jones vectors associated to the six basic polarized states are the following [12]:

SOP	Jones vector	SOP	Jones vector
LH $E_y = 0, E_{0x}^2 = 1$	$E_x = \begin{bmatrix}1\\0\end{bmatrix}$	LV $E_x = 0, E_{0y}^2 = 1$	$E_y = \begin{bmatrix}0\\1\end{bmatrix}$
L+ $E_x = E_y,$ $2E_{0x}^2 = 1$	$E_+ = \frac{1}{\sqrt{2}}\begin{bmatrix}1\\1\end{bmatrix}$	L− $E_x = -E_y,$ $2E_{0x}^2 = 1$	$E_- = \frac{1}{\sqrt{2}}\begin{bmatrix}1\\-1\end{bmatrix}$
RC $E_{0x} = E_{0y},$ $\delta_y - \delta_x = 90°$ $2E_{0x}^2 = 1$	$E_r = \frac{1}{\sqrt{2}}\begin{bmatrix}1\\+i\end{bmatrix}$	LC $E_{0x} = E_{0y},$ $\delta_y - \delta_x = -90°$ $2E_{0x}^2 = 1$	$E_l = \frac{1}{\sqrt{2}}\begin{bmatrix}1\\-i\end{bmatrix}$

The linear operation of any non-depolarizing optical device can be fully described by a 2 × 2 Jones matrix. A system of multiple devices distributed in a series setup can be straightforwardly modeled by multiplying the component Jones matrices to yield a single or equivalent system Jones matrix. Taking into account that the components of a beam emerging from a polarizing element are linearly related to the components of the incident beam, a relationship between them have been found by R. C. Jones [35], which is shown in the Eq. 2.38 [12]

$$E_x' = j_{xx}E_x + j_{xy}E_y, \tag{2.38a}$$

$$E_y' = j_{yx}E_x + j_{yy}E_y, \tag{2.38b}$$

where E_x' and E_y' are the components of the emerging beam, and E_x and E_y are the components of the incident beam. The Eq. 2.38 can be written in matrix form as the expression 2.39 [12]

$$\begin{pmatrix}E_x'\\E_y'\end{pmatrix} = \begin{pmatrix}j_{xx} & j_{xy}\\j_{yx} & j_{yy}\end{pmatrix}\begin{pmatrix}E_x\\E_y\end{pmatrix}, \tag{2.39}$$

where the Jones matrix is defined by $J = \begin{pmatrix} j_{xx} & j_{xy} \\ j_{yx} & j_{yy} \end{pmatrix}$.

It is important to mention that any Jones matrix can be expressed as a Mueller's matrix but in inverse it is not true. The Jones formalism applies only to non-depolarizing processes, where the incident light is totally polarized.

2.2.5.1 Jones matrix of a linear polarizer

The Jones vector for a linear polarizer can be represented by Eq. 2.40 [12]

$$\begin{pmatrix} E_x^{\prime} \\ E_y^{\prime} \end{pmatrix} = \begin{pmatrix} p_x & 0 \\ 0 & p_y \end{pmatrix} \begin{pmatrix} E_x \\ E_y \end{pmatrix} \qquad 0 \leq p_{x,y} \leq 1. \tag{2.40}$$

An ideal linear horizontal polarizer has a complete transmission in the horizontal *x*-axis ($p_x = 1$) and a complete attenuation along the vertical *y*-axis ($p_y = 0$), whereas a linear vertical polarizer has $p_x = 0$ and $p_y = 1$.

When a linear polarizer is rotated through an angle θ, its Jones matrix can be represented as a rotation transformation (Eq. 2.41), according to $\mathbf{J}^{\prime} = \mathbf{J}(-\theta)\mathbf{J}\mathbf{J}(\theta)$ where $\mathbf{J}(\theta)$ is the rotation matrix [12]

$$\boldsymbol{J}(\theta) = \begin{pmatrix} \cos\theta & \sin\theta \\ -\sin\theta & \cos\theta \end{pmatrix}. \tag{2.41}$$

Therefore, the Jones matrix for a rotated linear polarizer is given by Eq. 2.42 [12]

$$\mathbf{J}_{\boldsymbol{P}}(\theta) = \begin{pmatrix} p_x \cos^2\theta + p_y \sin^2\theta & (p_x - p_y)\sin\theta\cos\theta \\ (p_x - p_y)\sin\theta\cos\theta & p_x \sin^2\theta + p_y \cos^2\theta \end{pmatrix}. \tag{2.42}$$

2.2.5.2 Jones matrix of a linear retarder

A linear retarder increases the phase by $+\phi/2$ along the fast *x*-axis and retards the phase by $-\phi/2$, along the slow *y*-axis. The emerged electric fields are represented by Eq. 2.43 [12]

$$E_x^{'} = e^{+\phi/2} E_x, \tag{2.43a}$$

$$E_y^{'} = e^{-\phi/2} E_y. \tag{2.43b}$$

So, the Jones matrix for a retarder is represented by Eq. 2.44 [12]

$$\mathbf{J}_{\boldsymbol{R}}(\phi) = \begin{pmatrix} e^{+\phi/2} & 0 \\ 0 & e^{-\phi/2} \end{pmatrix}. \tag{2.44}$$

For a quarter-wave plate, $\phi = \pi/2$, and for a half-wave plate, $\phi = \pi$.

If the retarder is rotated an angle θ, with respect to the horizontal fast axis, the Jones matrix for this rotated retarder is given by Eq. 2.45 [12]

$$\mathbf{J}_{\boldsymbol{R}}(\phi, \theta) = \begin{pmatrix} \cos\frac{\phi}{2} + i\sin\frac{\phi}{2}\cos 2\theta & i\sin\frac{\phi}{2}\sin 2\theta \\ i\sin\frac{\phi}{2}\sin 2\theta & \cos\frac{\phi}{2} - \mathrm{i}\sin\frac{\phi}{2}\cos 2\theta \end{pmatrix}. \tag{2.45}$$

2.3 Spatially non-homogeneous or unconventional polarization states

While in the conventional polarization states study the behavior of the light based on the direction of the electric field oscillation and its spatial homogeneous distribution, the unconventional polarization is described via distributions of spatially non-homogeneous electric field, where the state of polarization does not depend on the spatial location in the beam cross section [9, 36-37]. Recently, there has been a special interest in the generation and application of unconventional polarization states of light as radial and azimuthal polarizations, and other types of polarization vortices and spatially engineered polarizations.

2.3.1 Cylindrical vector beams

A laser beam with cylindrical symmetry in polarization is known as cylindrical vector beam [9]. This kind of optical beams has spatially non-uniform polarization and describes vector beam solution of Maxwell's equations that obey axial symmetry both in the amplitude and the phase [9, 38-39].

The full vector wave equation for the electric field $\vec{E}$ is represented by the Eq. 2.46

[38]

$$\nabla\times\nabla\times\vec{E}-k^2\vec{E}=0. \tag{2.46}$$

There are solutions for the Eq. 2.46, which have spatially variant polarization state distributions across the beam section. When the axial symmetry to the beam-like vector solution for the Eq. 2.46 has the electric field aligned in the azimuthal direction, the solution of the electric field can be represented by the Eq. 2.47 [40, 41]

$$\vec{E}(r,z)=U(r,z)\exp[i(kz-\omega t)]\hat{e}_{\varphi}, \tag{2.47}$$

where $U(r,z)$ satisfies the Eq. 2.48 under paraxial and slow-varying envelope approximations, and $\hat{e}_{\varphi}$ is a unitary vector in the azimuthal direction [9, 41]

$$\frac{1}{r}\frac{\partial}{\partial r}\left(r\frac{\partial U}{\partial r}\right)-\frac{U}{r^2}+2ik\frac{\partial U}{\partial Z}=0. \tag{2.48}$$

The solution $U(r,z)$ with azimuthal polarization symmetry has a solution as Eq. 2.49 [9, 41]

$$U(r,z)=E_0J_1\left(\frac{\beta r}{1+\frac{iz}{z_0}}\right)\exp\left[-\frac{\frac{i\beta^2z}{2k}}{1+\frac{iz}{z_0}}\right]u(r,z), \tag{2.49}$$

where $J_1(\beta,r,z,z_0)$ is the first order Bessel function of the first kind, β is a constant scalar parameter, and $u(r,z)$ is the fundamental Gaussian solution given by Eq. 2.50 [9, 41]

$$u(r,z)=A\frac{w_0}{w(z)}\exp\left[-\frac{k}{2q(z)}r^2\right], \tag{2.50}$$

where $w(z)$ is the beam size, w_0 is the beam size at beam waist, $z_0=\frac{\pi {w_0}^2}{\lambda}$ is the Rayleigh range, and $q(z)=z+jz_0$ is the complex beam parameter.

Thus, the solution (Eq. 2.47) that corresponds to an azimuthally polarized vector Bessel-Gauss beam solution can be obtained through the Eq. 2.51 [9, 41]

$$\vec{E}(r,z) = E_0 J_1\left(\frac{\beta r}{1+\frac{iz}{z_0}}\right)\exp\left[-\frac{\frac{i\beta^2 z}{2k}}{1+\frac{iz}{z_0}}\right]u(r,z)\exp[i(kz-\omega t)]\hat{e}_\varphi. \qquad \textbf{(2.51)}$$

In the same form, the transverse magnetic field solution is represented by Eq. 2.52 [9, 41]

$$\vec{H}(r,z) = -\vec{H}_0 J_1\left(\frac{\beta r}{1+\frac{iz}{z_0}}\right)\exp\left[-\frac{\frac{i\beta^2 z}{2k}}{1+\frac{iz}{z_0}}\right]u(r,z)\exp[i(kz-\omega t)]\hat{h}_\varphi, \qquad \textbf{(2.52)}$$

where $\vec{H}_0$ is the constant magnetic field amplitude and $\hat{h}_\varphi$ is the unit vector in the azimuthal direction. This azimuthal magnetic field solution corresponding to an electric field in the transverse plane is aligned in the radial direction; therefore, Eq. 2.52 represents the radial polarization for the electric field.

The vector Bessel-Gauss at the beam waist can be approximated as Eq. 2.53 when β is very small [41]

$$\vec{E}(r,z) = E_0 r\exp\left(-\frac{r^2}{w^2}\right)\hat{e}_i \qquad i = r,\varphi. \qquad \textbf{(2.53)}$$

This approximation is the LG_{01} mode without the vortex phase term $\exp(-i\varphi)$ [42]. Cylindrical vector beams can be obtained by the superposition of two mutually orthogonal polarized Hermite-Gauss HG_{01} and HG_{10} modes [43] using the Eqs. 2.54 and 2.55

$$\vec{E}_r = HG_{10}\vec{e}_x + HG_{01}\vec{e}_y, \qquad \textbf{(2.54)}$$

$$\vec{E}_\varphi = HG_{01}\vec{e}_x + HG_{10}\vec{e}_y, \qquad \textbf{(2.55)}$$

where $\vec{E}_r$ and $\vec{E}_\varphi$ denote the radial and azimuthal polarization, respectively. The spatial distribution of the instantaneous electric field vector for some linearly polarized Hermite-Gauss and Laguerre-Gauss modes and the cylindrical vector modes are shown in Fig. 2.4. The states of polarization of the modes spatially homogeneous are represented in Fig. 2.4a, 2.4b, 2.4d, and 2.4e. The linear superposition of the radial and azimuthal polarizations are illustrated in Fig. 2.4c and 2.4f, respectively. Radial polarization has its instant electric field oscillating radially, while in the azimuthal polarization its instant electric field oscillates azimuthally or tangentially [9, 41].

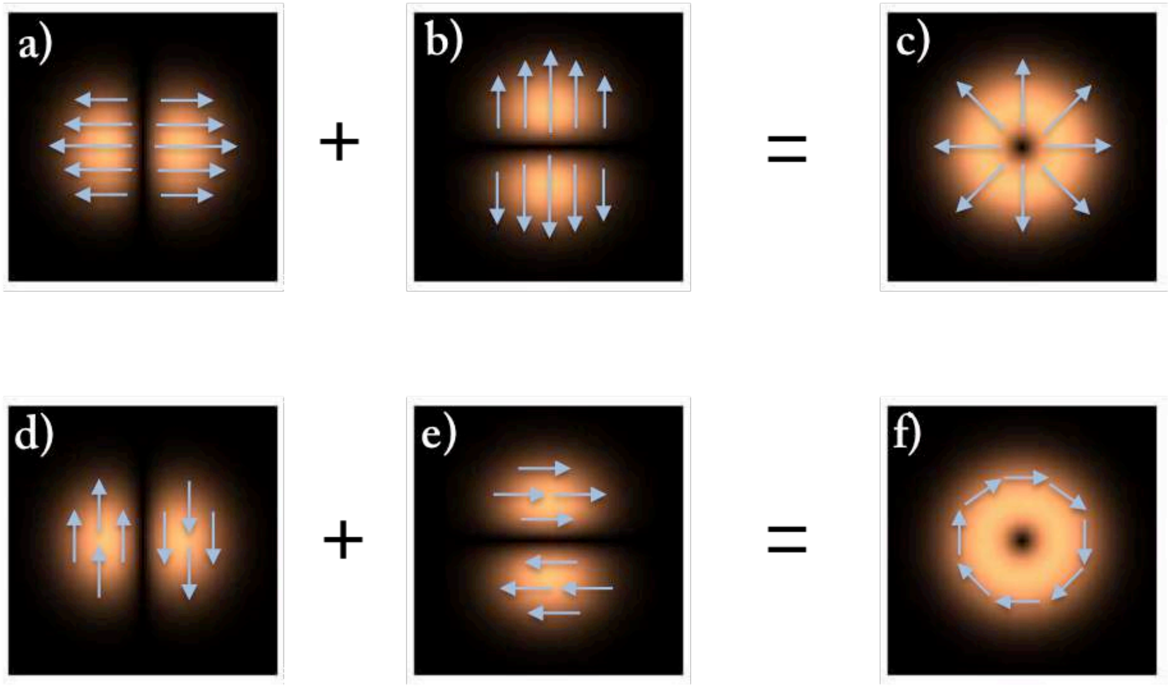

Fig. 2.4 Spatial distribution of instantaneous electric vector field for a) x-polarized HG$_{10}$ mode, b) y-polarized HG$_{01}$ mode, c) radially polarized mode, d) y-polarized HG$_{01}$ mode, e) x-polarized HG$_{01}$ mode, and f) azimuthally polarized mode.

2.3.2 Generation of radial and azimuthal polarizations

There are several methods to generate unconventional polarization states; they can be classified into two categories, active and passive methods [9].

To generate cylindrical vector beam it is necessary the use of the laser intracavity devices that force the laser to oscillate in cylindrical vector modes, this kind of methods are called active methods. Some intracavity devices as the axial birefringent or axial dichroic components can provide mode discrimination against the fundamental mode [44-47]. Intracavity interferometric methods can also generate cylindrical vector beams using mirrors or prisms based on the linear superposition principle [48].

On the other hand, passive methods transform spatially homogeneous polarizations (commonly linear or circular polarizations) into spatially inhomogeneous cylindrical vector polarizations [9]. This kind of methods can generate cylindrical vectors in free space using devices with spatially arranged retardation axis [49, 50], devices with continuous axial birefringence and dichroism [51, 52], employing liquid crystal (LC) materials [53] and LC spatial light modulators (SLM) [54]. The Mach–Zehnder interferometer combined with a spiral phase plate [55] could also generate cylindrical vector beams. Recently, a simple experimental method to generate radial and azimuthal polarization from the scattering of light by a metallic cylinder has been developed [56]. There are commercially available devices to convert linear or circular polarization into radial, azimuthal, and z-polarizations [57].

2.3.2.1 Radial polarizer converter

A commercially available polarizer that converts linear incident polarization beam into radial, azimuthal, or optical vortex beam is called S-wave plate (radial polarizer converter, Altechna) [58]. This device is a super-structured space-variant polarization converter fabricated by femtosecond laser writing of self-assembled nanostructures in silica glass [59]. Fig. 2.5 is the radial polarization converter.

Fig. 2.5 S-waveplate. Radial/Azimuth polarization converter (Altechna, RPC-515-06) [58].

The manufacturing process of the S-wave plate (SWP) consists of irradiating the volume of the glass with ultrashort laser pulses to form sub-wavelength nano-gratings [60] that act as a birefringent medium [61] and alters the polarization of the transmitted light. Due to the distribution of the nano-gratings within the volume of the glass, in such a way that the orientation of them depends on the azimuthal angle, complex polarization states can be generated. The cylindrical vector beams, either radial or azimuthal polarization beams, are formed depending on the polarization of the incident light.

According to the manual of the manufacturer of the S-wave plate [62], when the mark indicated in this device is parallel with the orientation of the linear incident polarization, the electric field direction of the emerged beam has the direction as show the Fig. 2.6a, that corresponds to the radial polarization. When the radially polarized beam is analyzed by linear polarizer with its transmission axis at 90°, 0°, +45°, and -45°, the intensity distribution of the radial polarization is illustrated in Fig. 2.6b-e, respectively.

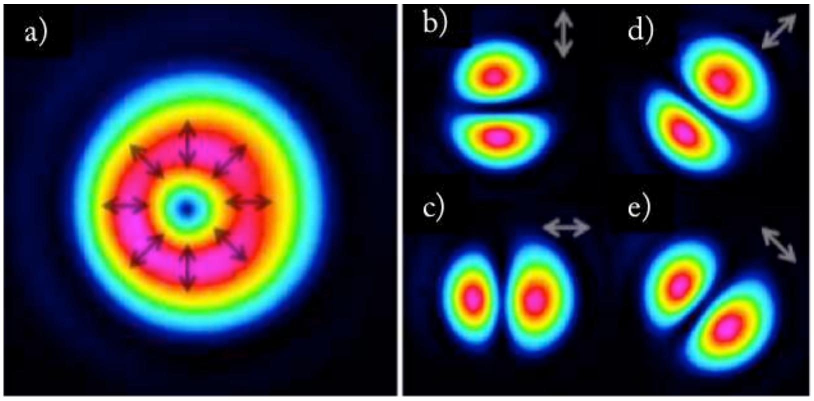

Fig. 2.6 Intensity distribution of the a) radial polarization beam measured with the camera CCD, and b-e) is the analyzed beam by linear polarizer with the transmission axis set at various angular positions (90°, 0°, +45°, and -45°, respectively) [62].

Following a similar procedure, the intensity distribution of the azimuthal polarization is illustrated in Fig. 2.7a and the beam analyzed by a linear polarizer with the transmission axis orientation at 90°, 0°, +45°, and -45° is shown in the Fig. 2.7b-e, respectively.

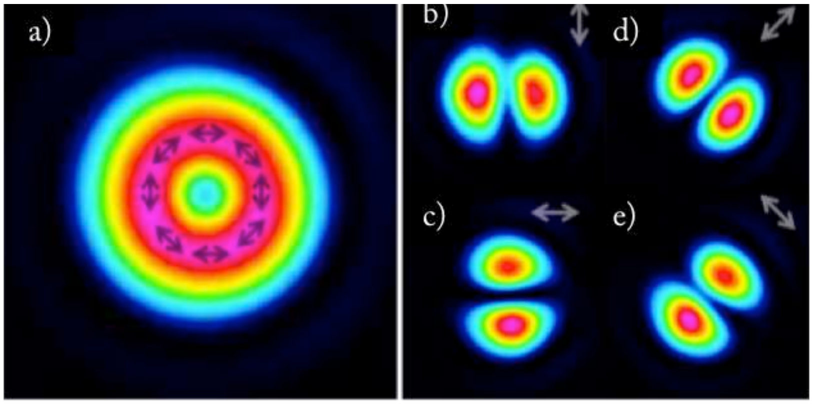

Fig. 2.7 Intensity distribution of the a) azimutal polarization beam measured with the camera CCD, and b-c) is the analyzed beam by linear polarizer (90°, 0°, +45°, and -45°, respectively) [62]

2.4 Polarimetry

The polarimetry techniques measure the change of the polarization state due to the interaction of the incident beam with matter and they are a powerful tool for optical characterization, imaging, and sensing applications [8, 63]. Thin films on surfaces, dielectric materials, biological samples and industrial micro-structures are some examples of the samples that can be characterized by polarimeters. This optical instrument is used to determine the polarization properties of samples as well as to test materials through to their corresponding the Mueller's matrix elements. To determine the 16 elements of this matrix it is necessary to analyze the polarization states of the reflected or transmitted light when the sample is illuminated with different known input polarization states, and it can be measured as a function of the wavelength and the angle of incidence. The Mueller's matrix polarimeter is composed of a polarization state generator (PSG), which produces the particular polarization state of the incident light, and a polarization states analyzer (PSA), which measures or analyzes the polarization state of the reflected or transmitted light by the sample shown in Fig. 2.8 [6, 64]. Linear polarizers and retarders are used both in the PSG and the PSA configuration setups to generate or analyze polarization state, respectively.

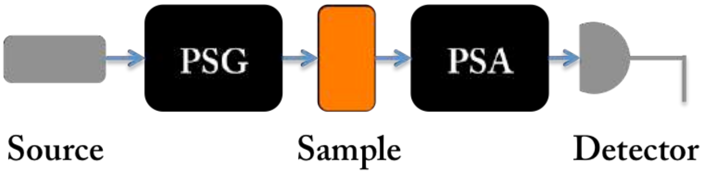

Fig. 2.8 Operational diagram of a general polarimeter arrangement (transmission configuration).

The polarization properties can be measured under transmission or reflection configurations. Fig. 2.8 shows the transmission configuration in which the PSA analyzes the transmitted light that passes through the sample; this kind of polarimeter primarily makes measurements on bulk samples (gas, liquid, solid) [64, 65]. In the reflection configuration (Fig. 2.9), the incident light is reflected at the interface between two optically different media and is analyzed by the PSA. The sample changes the incident polarization state due to the Fresnel reflection or transmission coefficients (explained in section 2.1) for the two linear polarizations, parallel (p) and perpendicular (s) to the incident plane. In the literature, the reflection polarimeter is normally called *ellipsometer* [64, 66] and is mainly used to measure optical properties of the plane or smooth interfaces and thin films.

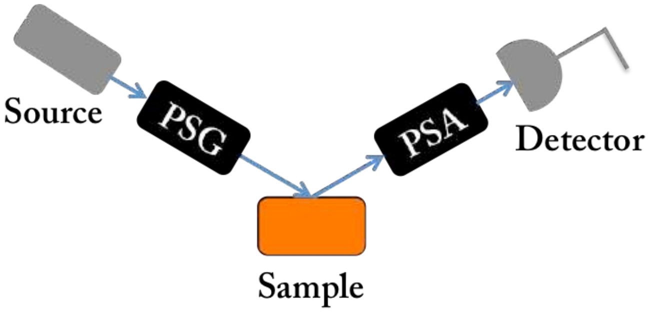

Fig. 2.9 Polarimeter under a reflection configuration.

A reflection polarimetry has been employed to develop part of this thesis. For this reason, some variants of the polarimeter arrangement with this configuration are explained in the following paragraphs.

A reflection polarimeter that uses a source to illuminate the sample at some fixed angle of incidence, within a range of wavelength in the ultraviolet/visible region, is called spectropolarimeter (SE) [67-69], but there exists a multiple-angle-of-incidence (MAIE) polarimeter [70, 71] that measures the reflected light at several angles of incidence. Combining simultaneously both polarimeters that make the measurements at multiple-angles-of-incidence and at several wavelengths, an instrument that is named variable angle spectroscopic ellipsometer (VASE) [72] is obtained. On the other hand, there exist polarimeters to measure the reflected light with a detector, which may be a photodiode or photomultiplier [73], but it has been recently developed the imaging polarimetry using a CCD camera [5, 74].

2.4.1 Micro-polarimetry

A limitation of polarimetric systems is the spot size of illumination because some of them are in the range of 3 to 1 mm in diameter. If the sample size is smaller than the spot size want to be measured, it can not be accurately discriminated. Particularly, when the samples are inhomogeneous or aperiodic nanostructures (target gratings), the averaged analysis will lead to incorrect results. The developing of the micro- and nano-structures implies making measurements within micro-spot sizes, typically between 50 and 25 μm [74-76], thus to solve this issue a microscope objective lens has been incorporated to focus the incident light with a micro-spot size on the sample. The system is called Mueller-matrix micro-polarimeter, which obtains imaging static samples providing well-defined reflection properties of the material. This technique can angularly resolve the Mueller matrix of the micro- and nano-structures using a high numerical aperture (NA) microscope objective [77, 78], and can characterize transparent samples [79, 80] obtaining the corresponding ellipsometric parameters (ψ, Δ) that represent the amplitude ratio ψ and phase difference Δ between light waves known as p- and s-polarized light waves [64, 68], and then calculate the refraction index or thickness of the sample [81].

2.4.2 Microscope objective lens

Inserting a microscope objective lens in a polarimetry system allows capturing the angular distribution of the light coming from the sample, which is actually mapped on the objective back focal plane [80, 82]. Due to Abbe's sine condition [8], a parallel beam emerging from the sample with a polar angle θ and an azimuth φ is focused in the back focal plane on a point with radial coordinates $(f \sin\theta, \varphi)$, where f is the objective focal length (Fig. 2.10).

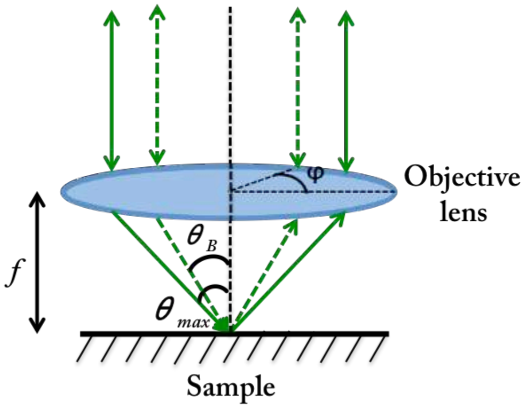

Fig. 2.10 Side view of a collimated illumination field focused into a sample.

The azimuth angles ranging from 0° to 360°, and the polar angles θ are limited by the NA of the objective. The maximum angle of incidence (θ_{max}) is calculated through the numerical aperture of the objective lens (the sine condition), Eq. 2.56 [8]

$$NA = \sin\theta_{max}. \tag{2.56}$$

The maximum radius R_{max} of the exit pupil image is obtained according to by Eq. 2.57 [8]

$$R_{max} = f \sin\theta_{max}. \tag{2.57}$$

The relationship between an arbitrary distance R from the image center and its corresponding incidence angle θ_a can be calculated using the Eq. 2.58

$$\sin\theta_a = \left(\frac{R}{R_{max}}\right)\sin\theta_{max}. \tag{2.58}$$

2.4.3 Multiple-angle-of-incident using a microscope objective lens

In the previous section 2.4 was mentioned there exist reflection polarimeters that measure the reflected light at several angles of incidence. These systems make measurements for each angle of incidence, and this implies investing time to complete all the required measurements in a range of 15°-90° incidence angles [83]. A microscope objective lens with high NA is able to illuminate the sample at several incidence angles in a single shot (Fig. 2.10). When a high NA lens obeying sine-condition focuses the incident light into a small spot on the surface of the sample (Fig. 2.10), the maximum angle of incidence θ_{max} is calculated through the Eq. 2.56. The focal length of the lens is calculated by $f = R_{max}/NA$ [8]; thus if the NA of the objective lens increases, the corresponding focal length reduces. A high NA aperture objective lens allows measuring the data with better sensitivity because there is not Fresnel contribution at the Brewster angle from the sample, meaning the Fresnel coefficients at this angle are zero [84, 85].

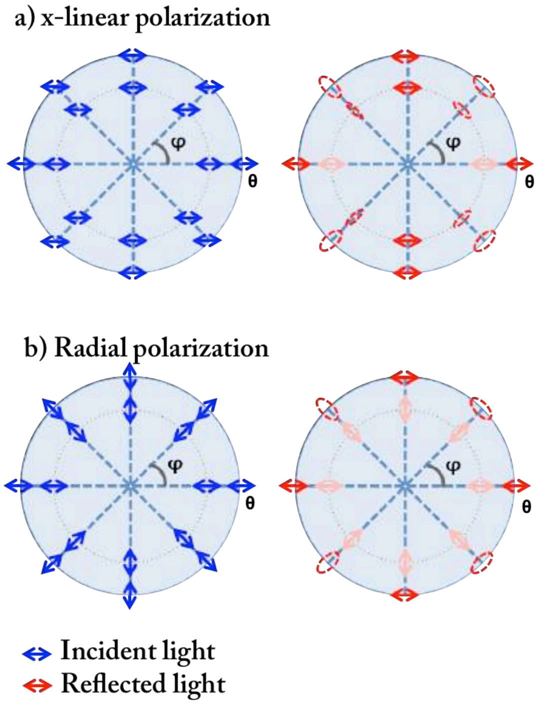

Fig. 2.11 Multiple rays incidence with a) x–linear and b) radial polarization at different angles of incidence by an objective lens. Blue and red arrows represent the incident and reflected rays, respectively.

The behavior of the polarized illumination field coming into an objective lens is illustrated in Fig. 2.10. The angle between the direction of the each incident electric field and its corresponding local incidence plane has a geometrical dependence with the azimuthal position (φ). This effect is shown in the Fig. 2.11a, each incident x-linear polarized ray (blue arrow) has a local incident plane (blue dotted line), thus the reflected intensity distribution decreases to zero where the direction of the electric field coincides with the direction of its local incident plane and the ray strikes at the Brewster's angle. On the other hand, when the incident beam is radially polarized (Fig. 2.11b), the electric field direction of this beam is always in the plane of incidence and hence it is seen as a linear x-polarization for any azimuthal angle (φ). Therefore, the reflected intensity distribution decreases to zero at the Brewster angle associated to the dielectric surface under study.

Chapter 3 Experimental results and discussions

In this Chapter, the experimental results using conventional and unconventional polarization states to study the polarimetric behavior of the light when interacting with certain systems are discussed. In the first part, the experimental determination of the angularly resolved Mueller's matrix (MM) associated to the light scattered by a metallic cylinder using conventional polarization states is reported; in the second part, the methodology to measure the refractive index of a dielectric sample using highly focused radial and parallel polarized light is explained, and the experimental and theoretical results are compared and discussed.

3.1 Polarization properties of light scattered by a metallic cylinder

In this section, an experimental validation to prove that the angularly resolved Mueller's matrix associated to a metallic cylinder is similar to a one-dimensional surface Mueller's matrix is reported. Furthermore, from the experimental Mueller's Matrix elements were determined the main scalar polarization metrics associated to light scattered by a metallic cylinder, when the illumination is perpendicular to the cylinder axis.

3.1.1 Preliminary study of a metallic cylinder

A cylinder with an axis oriented along the y-axis is also a highly symmetric system that can be considered as the minimum expression of what builds a 1D surface, a single groove [86]. A one-dimensional (1D) rough surface is a highly symmetric system, defined with respect to a Cartesian coordinate system as a surface whose profile (z-axis) varies only along the x-axis and is constant along the y-axis. The scattering properties of 1D rough metallic and dielectric surfaces have been extensively reported theoretically, numerically, and experimentally [17-21, 87-91] and the polarimetric behavior has been reported using the Mueller-Stokes formalism [4, 12, 17-21].

Due to its potential applications to many problems in radiative transfer, remote sensing, diagnosis, and particularly in the forensic analysis of fibers, cylinders have been one of the main geometries studied [16, 86, 92-99]. Of particular importance has been the work done on the aspect ratio dependence of the light scattered by cylinders [86, 92]. Some authors have applied simple models based on the geometrical theory of diffraction to obtain the diffraction pattern of the scattered light and then have calculated the cylinder diameter [98, 99]. Experimental and theoretical studies related with the scattering of light by cylinders have been reported (optical fiber with an evaporated thin film), where the elements of the Mueller's matrix have been measured within an angular interval of 180°, but neither the polarization behavior as a function of the scattering angle nor their potential applications have been discussed [100-101]. Recently, the scattering of light by cylinders under a conical geometry of incidence has given rise to a method to generate radial and azimuthal unconventional polarization states [56]. Extensive theoretical and numerical work have reported the diffraction and scattering of light by metallic cylinders illuminated under both, plane and conical geometries of incidence, using linear polarizations parallel and perpendicular to the cylinder axis [24, 54, 86, 92-97, 98-101]. Eq. 2.22 is the polarimetric model that best describes the light scattered by the metallic cylinder illuminated perpendicularly to the cylinder axis [100, 101].

3.1.2 Experimental arrangement.

Employing a HeNe laser (632.8 nm), a polarization state generator (PSG), and a polarization state analyzer (PSA), a collimated beam with 2 mm wide was generated and sent towards the metallic cylinder at normal incidence. As a way to show the simplicity of the system, an electric guitar string was employed as the metallic cylinder, placed at the center of an automated rotation stage of an angle-resolved scattering system (ARS), Fig. 3.1 The cylinder is a commercially available electric guitar nickel string, with a 254 μm diameter (Fender, 3150R Pure Nickel String, 0.01 inch diameter). The nickel has a refractive index of 1.98+i3.74 [102] and a skin depth of 0.013 μm to 0.633 μm wavelength, which ensures the illuminating light is not transmitted through the cylinder. The polarization state generator (PSG) consists of a linear polarizer of the Glan-Thompson type (Thorlabs, GTH10M), followed by a liquid crystal variable retarder and its controller (Thorlabs, LCC1111-A and LCC25, respectively), both mounted in motorized rotation stages (Thorlabs, PRM1Z8E). The polarization state analyzer (PSA) is a commercially available head (Thorlabs, model PAX5710/VIS), which is mounted on a 40-cm-long arm and pointed toward the illuminated spot at the center of the cylinder. The experimental error of the complete system, including the laser fluctuations, is of the order of a 4% [103].

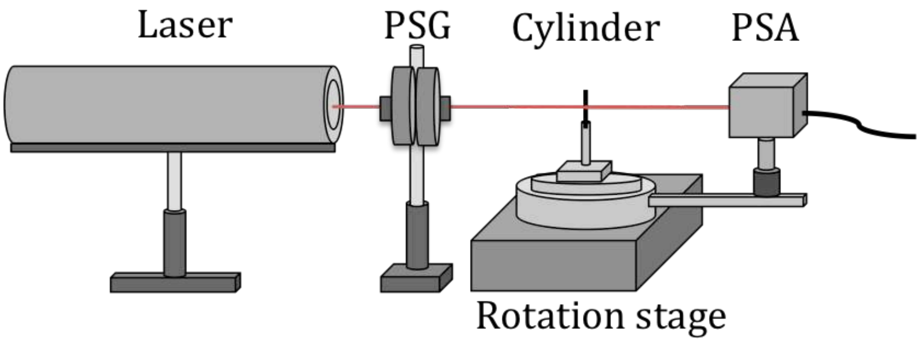

Fig. 3.1 Experimental setup employed for the measurement of the light scattered by the metallic cylinder.

The scattered light is distributed on a plane surface, perpendicular to the cylinder axis. To obtain the Mueller's matrix, a set of six polarization states was employed (linear horizontal, perpendicular, to +45°, -45°, and circular right- and left-handed polarization states, respectively). In the absence of any polarization-sensitive effect in the optical medium placed between the PSG and the PSA, the experimental setup was verified in order that each state of polarization detected corresponds to the same state of polarization generated.

3.1.3 Results and discussion of the experimental Mueller matrix of the metallic cylinder

The 36 angularly-resolved measurements of intensity were handled by applying an algebraic algorithm to the data obtained [104, Appendix A1], in order to get the 16 Mueller's matrix parameters, which were plotted versus the scattering angle $0° < \theta_{scatt} < 360°$. The Mueller matrix parameters are shown in Fig. 3.2, where the data corresponding to angles in the vicinity of the direction of propagation, $\theta_{scatt} = 180°$, have been omitted due to saturation present on the detector (stops or neutral spatial filters have not been used to cancel or attenuate the beam in that direction). In Fig. 3.2, the angularly-resolved Mueller matrix elements show that $m_{00} \cong m_{11}$, $m_{01} \cong m_{10}$, $m_{22} \cong m_{33}$, $m_{23} \cong -m_{32}$, and the elements m_{02}, m_{03}, m_{12}, m_{13}, m_{20}, m_{21}, m_{30}, $m_{31}$are almost zero. They are not exactly zero, probably due to the fact that the commercial guitar string has some surface defects that scatters and polarizes the light slightly. If the matrix elements that should be zero-valued are neglected, we can conclude that the measured Mueller's matrix (MM) of Fig. 3.2 confirms the model, Eq. 2.22. This is not an obvious result because a one-dimensional rough surface with any arbitrary profile is not a single cylinder.

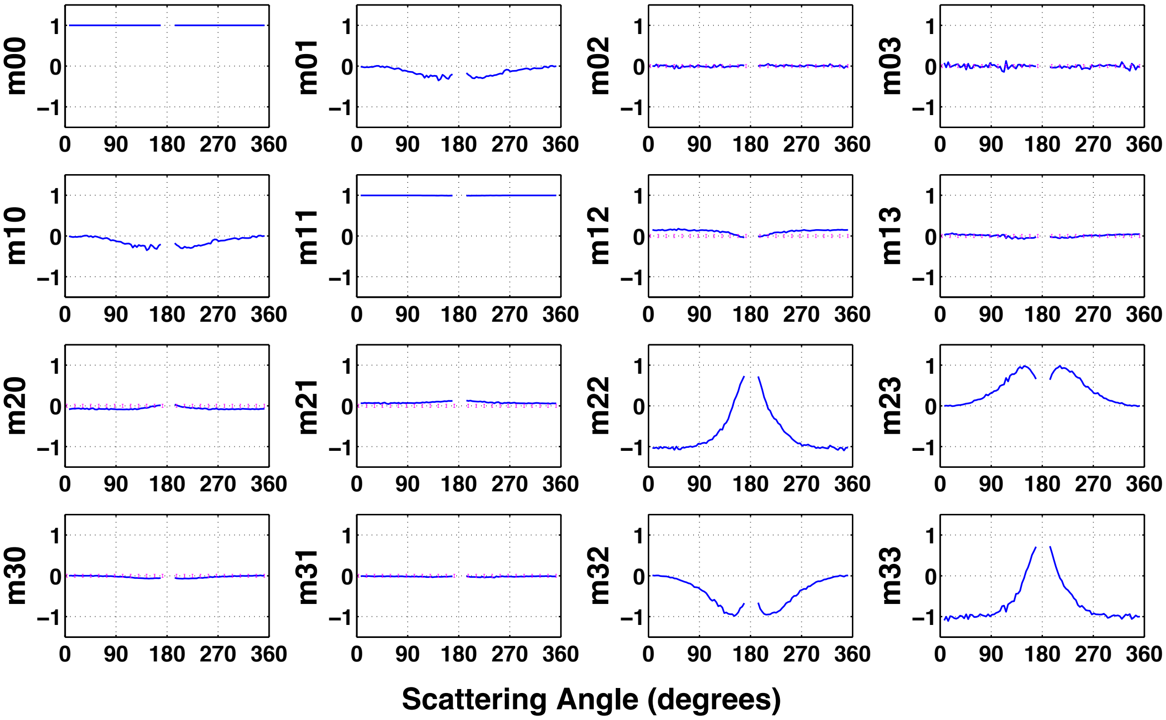

Fig. 3.2. Normalized Mueller's matrix elements versus the scattering angle ($0° < \theta_{scatt} < 360°$), associated to the scattering of the light by a metallic cylinder. It is possible to observe $m_{00} = m_{11}, m_{01} = m_{10}, m_{22} = m_{33}, m_{23} = -m_{32}$. The experimental error is represented by vertical bars (±4%).

3.1.4 Results and discussions of the main polarimetric parameters of the metallic cylinder

Employing the MM values obtained from Fig. 3.2, some of the main polarimetric parameters have also been computed. The Fig. 3.3 shows the depolarization index, Eq. 2.28, the Gil-Bernabeu theorem, Eq. 2.33, the diattenuation, Eq. 2.31, and the polarizance parameters, Eq. 2.30, respectively. All of them plotted in terms of the scattering angle (degrees).

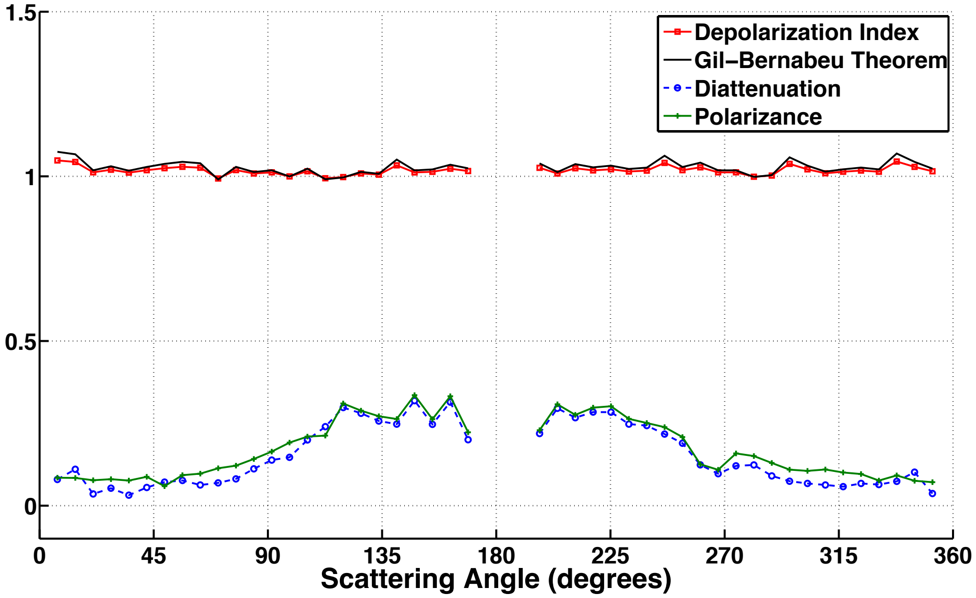

Fig. 3.3 Polarization scalar metrics versus the scattering angle. Depolarization index (–■–), the Gil-Bernabeu theorem (––), the diattenuation (–O–) and the polarizance (–+–) parameters, respectively.

The depolarization index, (–■–), takes on values around 1, with small oscillations, according to the resolution of the experimental setup employed here. The plot of the Gil-Bernabeu theorem, (––), shows the same behavior than the depolarization index; note also that the MM of Fig. 3.2 satisfies Eq. 2.33, the necessary and sufficient condition for a MM to be a Mueller-Jones matrix (represented as the ratio of the left-hand side divided by the right-hand side of Eq. 2.33). At this stage, it is important to point out that a fully polarized incident beam is being used. It is well known that a 1D surface depolarizes light when multiple scattering effects are being present (under normal incidence), which is the case if the totally polarized incident light is scattered around 180° for a perfectly reflecting surface [20] or around 360° for a reflecting and transmitting surface. The results obtained here by applying the depolarization index or the Gil-Bernabeu theorem, prove there are not depolarization effects or if they are present, their contribution is within our experimental error complete system. In addition, by taking into account that each Mueller parameter m_{ij} is originated from the sum of four different and independent intensity measurements, probably the variation from the unity value for the depolarization index and the Gil-Bernabeu theorem, are originated by statistical speckle noise presented during the scattering process. Another error factor can be due to the possible multiple reflections from the internal walls inside the PSA head before reaching the detector (diameter size of 3 mm).

On the other hand, the diattenuation, Eq. 2.31 and the polarizance parameters, Eq. 2.30, have almost the same, slowly varying and symmetric behavior, with average maximum values of 0.25 around $80° < \theta_{scatt} < 180°$and $180° < \theta_{scatt} < 280°$ and with average minimum values of 0.08 around $0° < \theta_{scatt} < 80°$ and $280° < \theta_{scatt} < 360°$. This means that the metallic cylinder can polarize un-polarized incident light, with an efficiency that depends on the scattering angle. Considering that $m_{01} = m_{10}$, $m_{20} = m_{30} = m_{02} = m_{03} = 0$, Eqs. 2.30 and 2.31 can be reduced approximately to a same angular behavior, $P(M) = m_{01}/m_{00} \cong m_{10}/m_{00} = D(M)$.

3.2 Refractive index measurement using x-linear and unconventional radial polarized light

In this section, a method to measure the refractive index of the dielectric sample through determining the Brewster's angle is proposed. This method uses a polarimetric instrument that measures, in a single shot, the intensity of the reflected light by the sample at the back focal plane, for incidence angles ranging from 0° to 64° and all azimuths angles around a full circle, when the sample is illuminated by highly focused radial polarization. x-linear polarization state also was used with the aim to compare with the radial polarization result. Experimental and theoretical results are compared to validate the method.

3.2.1 Preliminary study of the refractive index measurement

The refractive index is an essential optical parameter for the characterization of micro-structures. Several optical techniques used to measure the refractive index of the thin films and dielectric materials have been developed through analyzing the transmitted and reflected light by the sample. The ellipsometric methods measure the change of polarization of the light reflected or transmitted by a surface [64, 71] but the typical spatial resolution is poor and the spot size is around millimeters. Therefore several, approaches have been developed to increase the spatial resolution of conventional ellipsometers [76, 105-106]. Some experimental methods for determining the refractive index of dielectric surfaces by using the polarization of light reflected near the Brewster's angle of the sample under study have been proposed [107, 108], but the precision is not good enough. The polarized reflectance measurement technique for thickness and index (PRETTI method) allows one to obtain the refractive index and thickness of a thin film by using S-polarized (linear polarization perpendicular to the plane of incidence) and P-polarized (linear polarization parallel to the plane of incidence) reflectances, measured at oblique angles of incidence [109]. The prism coupling method is only applicable to thin samples [110]. The Abbe refractometer is based on the critical angle method, therefore it is not applicable to samples of refractive index larger than its coupling prism [111]. The minimum deviation method is typically used for bulk materials, but the samples have to be prepared prism-shaped, which are difficult to measure [112]. Another method combines an optical low-coherence interferometer and confocal optics to make simultaneous measurements of the phase index, the group index, and the geometrical thickness of an optically transparent object [113-115], but it is very sensitive to the optical path difference and requires complex instrumentation. Most of those methods demand a lot of time to make measurements; furthermore, the experiment arrangements are sophisticated, the beam spot size is large and lacks spatial resolution, and have a high price.

3.2.2 Spatial Average Symmetry associated to radial and azimuthal polarization.

Before illuminating the sample, it was necessary to verify the quality of the radial and azimuthal incident light generated by the S-wave plate [58], testing the Spatial Average Symmetry (SAS) associated to the cross section of unconventional polarized light by the Eq. 3.1 [116]

$$\langle S\rangle_{spa} = [S_0 \;\; S_1 \;\; S_2 \;\; S_3]^T, \tag{3.1}$$

where ⟨ ⟩ represents the spatial average operation and T denotes the transpose matrix operation.

To obtain the Stokes parameters, the relationships of Eq. 2.19 were used and it was assumed that they are also valid for images (intensity spatially distributed) registered by a CMOS camera when a quarter-wave plate (QWP), a half-wave plate (HWP), and a linear polarizer (LP) are used to analyze the contribution from the radial and azimuthal polarizations. Fig. 3.4 shows the experimental setup employed to generate radially and azimuthally polarized beams and to analyze their contribution to the six basic polarization states (x parallel, y vertical, +45, -45, circular right- and circular left-handed polarization).

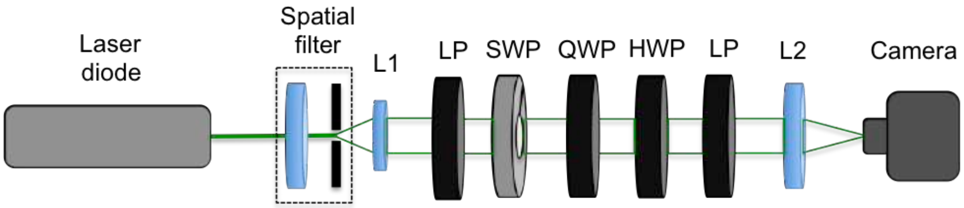

Fig. 3.4 Schematic diagram employed for the experimental determination of the Spatial Average Symmetry associated to unconventional polarized beams of light (taken from [116]). A light beam is spatially filtered and then collimated by lens L1; LP represents a linear polarizer; SWP represents the S-waveplate converter; QWP and HWP represent quarter- and half-waveplates, respectively; L2 is a lens employed to form an image on the plane of a CMOS camera.

“A laser diode is employed as the source of monochromatic light (Thorlabs, laser diode model DPSS, @532 nm), which is spatially filtered to produce a uniform intensity, and it is collimated by a lens L1. A linear polarizer with its transmission axis parallel to the optical table generates a conventional linear polarization incident at the S-waveplate (Altechna, model RCP-515-06), which generates the unconventional polarizations reported here, except along the optical axis, where there exists a singularity [117]”, [116].

Fig. 3.5 shows the intensity spatial distribution of unconventional polarization beams generated by the S-wave plate and detected by the CMOS camera (Thorlabs, DCC3240C). Fig. 3.5a and Fig. 3.5b represent the total intensity measured directly by the camera for the radial and azimuthal polarization beams, respectively. Observe that both radial and azimuthal polarizations generated are not perfectly symmetric, even when a collimated linearly polarized beam with uniformly intensity was incident on the polarization converter.

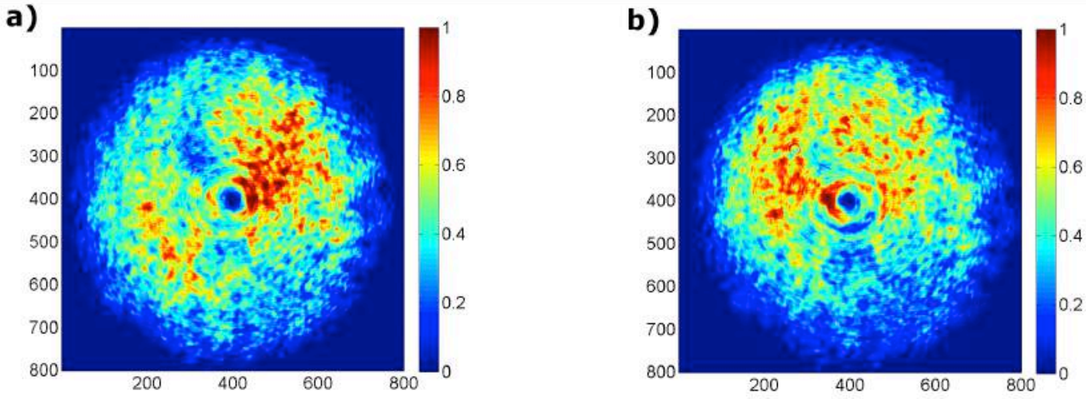

Fig. 3.5 Intensity spatial distribution of a) radial and b) azimuthal polarization beams generated by the S-wave plate.

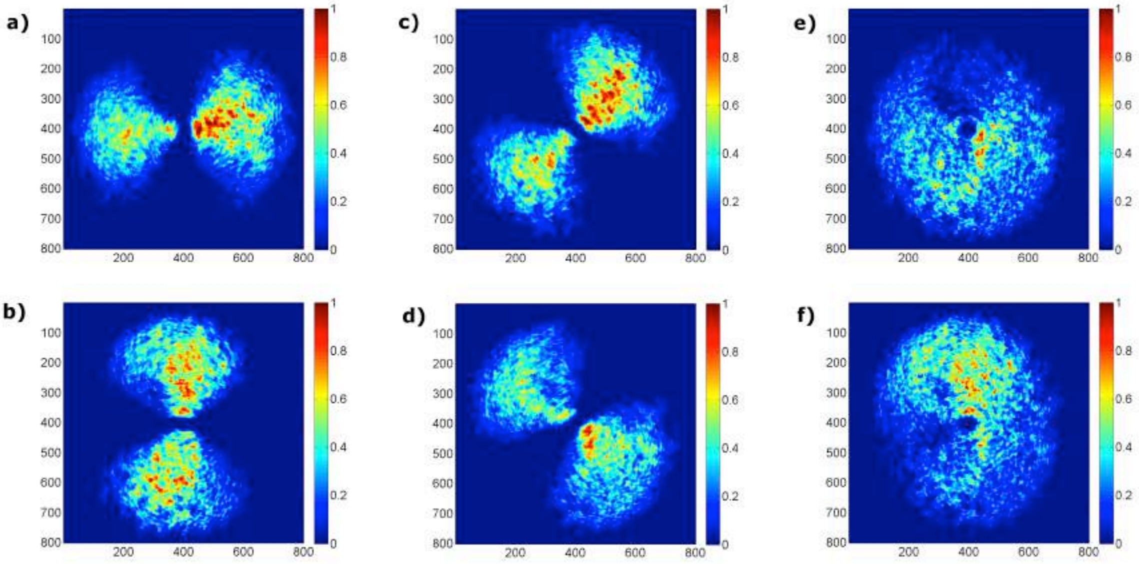

Fig. 3.6 Intensity spatial distribution analyzing a) x, b) y, c) +45, d) -45, e) circular right-, and f) circular left-handed polarizations associated to a radial polarization beam.

Fig. 3.6 and 3.7 show the intensity distributions when radial and azimuthal polarization beams, respectively, were analyzed their contributions to x (Fig. 3.6a and 3.7a), y (Fig. 3.6b and 3.7b), $+45$ (Fig. 3.6c and 3.7c), -45 (Fig. 3.6d and 3.7d), r (Fig. 3.6e and 3.7e), and l (Fig. 3.6f and 3.7f) polarization states. Comparing the images of the Figs. 3.6a-d and 3.7a-d with the images provided by the manufacturer of the S-wave plate [62] shown in Figs. 2.6b-e and 2.7b-e, it can be observed that the obtained experimental images have more symmetry and their spatial distribution are more symmetric. It is important to mention that the intensity depends on the exposure times; the images were registered trying to avoid saturation. Similar images were taken several times, with different exposure times, exhibiting high reproducibility.

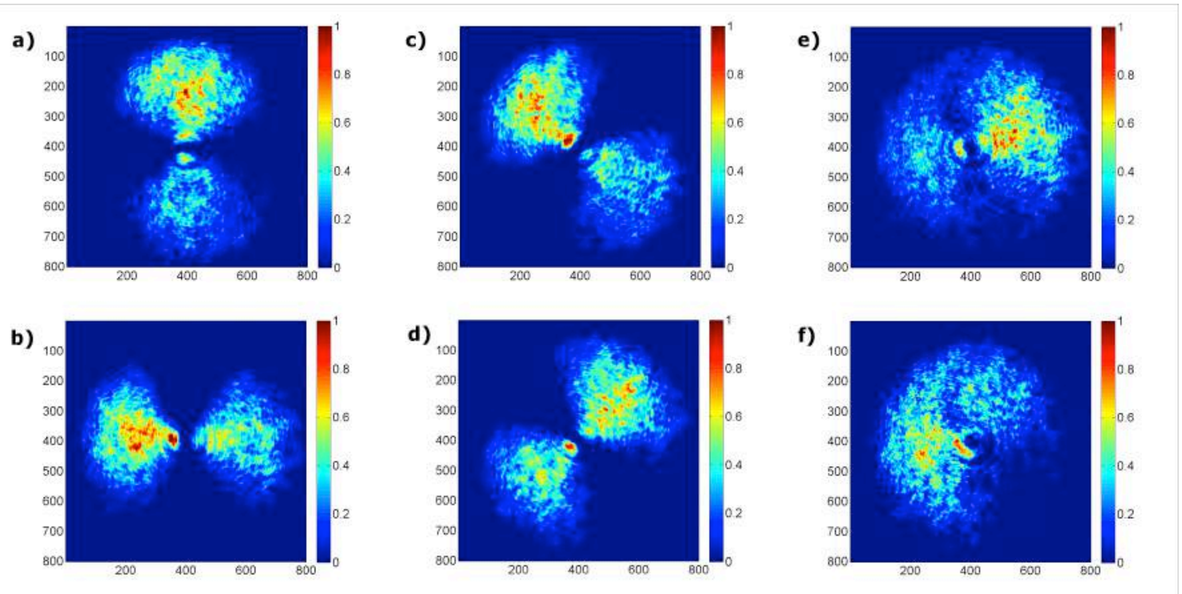

Fig. 3.7 Intensity spatial distribution analyzing a) x, b) y, c) +45, d) -45, e) circular right-, and f) circular left-handed polarizations associated to an azimuthal polarization beam.

The Stokes parameters, represented by images, for both azimuthal and radial polarizations were obtained by applying the Eq. 2.19 to the beam generated and the spatial average symmetry, Eq. 3.1 were calculated by using a Matlab code [Appendix A2].

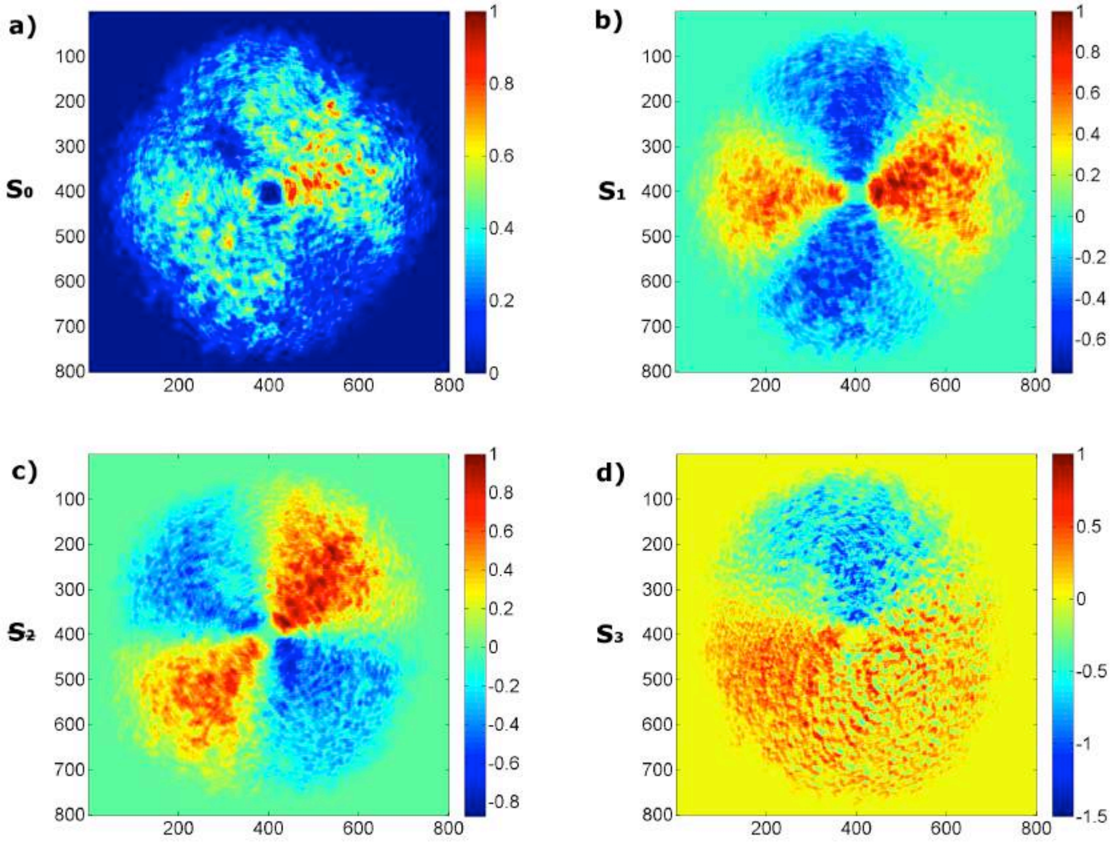

Fig. 3.8 Stokes parameters associated to experimental radial polarization mode a) S0, b) S1, c) S2, d) S3. Spatial average symmetry, $\langle S\rangle_{spa} = [1.0000 \quad 0.0021 \quad 0.0244 \quad 0.1562]^T$. Values are plotted in terms of pixels and the intensity values have been normalized.

Figure 3.8 shows the normalized experimental Stokes parameters for radially polarized light. Fig. 3.8a is associated to the S_0 total intensity measured according to Eq. 2.19; “note it is not axially symmetric, but shows only positive values, as expected for the total intensity distributed spatially. All the Stokes parameters reduce their intensities with respect to the original image, due to the attenuation present within the polarization state analyzer setup (Fig. 3.4)”. This intensity reduction is clearly noted in the S_0 element, Fig. 3.8a. Figs. 3.8b and 3.8c represent the second and third Stokes elements, respectively, are very similar, except one is rotated to 45° with respect to the other. The Stokes element S_3, Fig. 3.8d, shows spatial contributions to both, right- and left-hand polarizations. Note a visual appreciation does not allow determine if there exists some preferential or dominant polarization associated to Figs. 3.8, this is only qualitative information. “This means that even when the experimental determination of the Stokes vector images provides more information, it is not conclusive, because it lacks numerical evaluations which provides the average tendency followed by the polarization analyzed”. On the other hand, the use of the SAS defined by Eq. 3.1, plays a very important role, because it allows one to compute every Stokes image parameter to get the complete Stokes vector. The spatial average of the Stokes image parameters over the area of the image, Fig. 3.8, provides $\langle S \rangle = [1.0000 \quad 0.0021 \quad 0.0244 \quad 0.1562]^T$. Note there is not perfect axial symmetry for the experimental radial polarization mode, even when the Stokes spatial average tendency is an elliptical right-hand polarization.

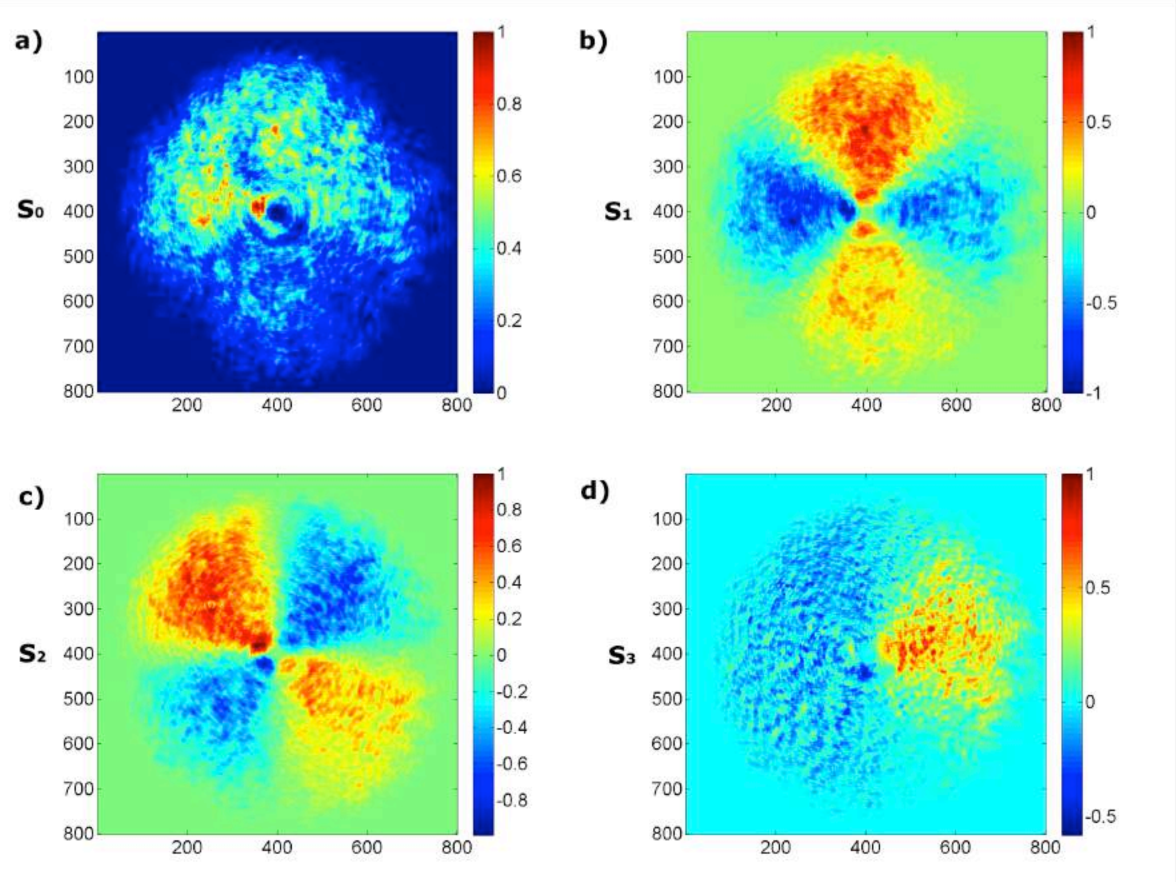

Fig. 3.9 Stokes parameters associated to the experimental azimuthal polarization, a) S_0, b) S_1, c) S_2, d) S_3. Spatial average symmetry, $\langle S \rangle_{spa} = [1.0000 \quad 0.0923 \quad 0.1043 \quad -0.0827]^T$. Values are plotted in terms of pixels and the intensity values have been normalized.

Figure 3.9 shows the normalized experimental Stokes parameters for azimuthally polarized light. The Stokes parameter S_0, Fig. 3.9a, exhibits also the effect of the intensity diattenuation due to the linear analyzer. The Fig. 3.9b represents S_1, with both positive and negative contributions to the intensity spatial distribution. Fig. 3.9c shows the contribution to linear 45°, -45° polarizations. Finally, Fig. 3.9d shows the radial polarization contribution to circular polarization. Once again, Fig. 3.9 provides only qualitative information. The quantitative information to the experimentally determined Stokes image parameters for generated azimuthal polarization is $\langle S\rangle_{spa} = [1.0000 \quad 0.0923 \quad 0.1043 \quad -0.0827]^T$. The result obtained shows a Stokes spatial average tendency associated to a slightly elliptical left-hand polarization state. In this case, this means the azimuthally polarized mode beam does not exhibit a perfectly axially symmetric polarization distribution, a fact that is consistent with the image associated to the Stokes element S_0 (Fig. 3.9a).

Those results show that the S-wave plate does not generate a perfectly a radial or azimuthal polarization. This is important to keep in mind because the following measurements were made using this device.

3.2.3 Theoretical images of the reflected beam by the sample

To produce theoretical images of the beam reflected by the sample, matrices for the incident electric field distribution at the horizontal and vertical orientations were defined. Due that the incident field ($\vec{E}^i$) is focused onto the surface of the sample; it was projected in the plane of incidence to calculate its parallel (or P) component, as Eq. 3.2a,

$$E_p^i = \vec{E}^i \cdot \hat{r} \tag{3.2a}$$

where $\hat{r}$ is the radius vector associated to the azimuthal angle φ. On the other hand, the perpendicular (or S) contribution is realized according to the following Eq. 3.2b,

$$\vec{E}_s^i = \vec{E}^i - E_p^i \hat{r} \tag{3.2b}$$

Once the field components (Eq. 3.2) have been obtained, the reflected beam can be found via the Fresnel coefficients, r_p and r_s, by the Eq. 3.3 [8],

$$E_p^r = r_p E_p^i \tag{3.3a}$$

$$E_s^r = r_s E_s^i \tag{3.3b}$$

Fig. 3.10 shows theoretical reflectance images generated numerically for the BK7 glass when it is illuminated with x-linear and radial polarization, respectively. In the simulation, a uniform light source and a homogeneous and isotropic sample were considered. After obtaining these images, the position of the Brewster's angle was found and compared with the experimental values. To extract the Brewster's angle, for each image, the pixel position (x_m, y_m) where the intensity is minimum was identified. Then, the distance r between the center of the image and the position (x_m, y_m) was calculated through $r = \left|({x_m}^2 + {y_m}^2)^{1/2}\right|$, and finally, the Brewster's angle was obtained by means of $sin(\theta_B) = r/f$ where f is defined by the Eq. 2.57. This value allows the calculation of the Brewster angle and hence the refractive index of the sample. In the Appendix A3 is shown the MATLAB algorithm used to determine the Brewster's angle.

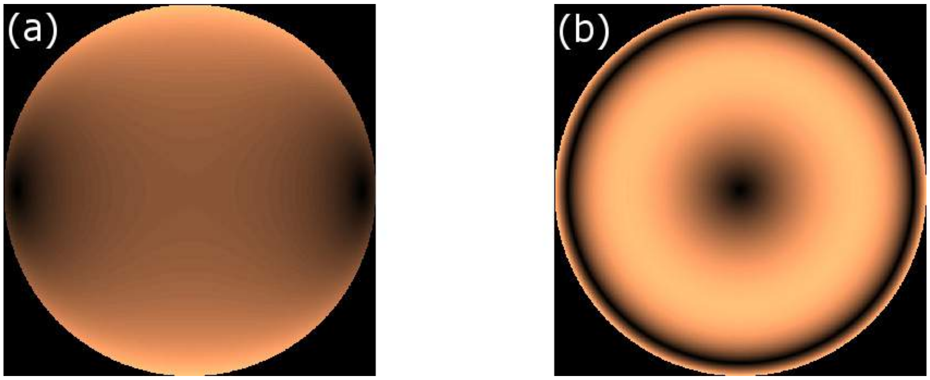

Fig. 3.10 Theoretical images generated numerically considering a homogeneous and isotropic BK7 glass sample. Incident beam: (a) x-linear and (b) radial polarization.

3.2.4 Experimental images of the reflected beam by the sample

The experimental setup is illustrated in Fig. 3.11. A beam generated by an unpolarized laser (Melles Griot, Model 05-LGR-193-381 @543.5 nm) is spatially filtered (Newport, Model 910A) and collimated by a lens (L1). It passes through of the polarization state generator (PSG) and ends up focused by the objective lens, OL, (Nikon, Tu Plan Fluor EPI P 100x/NA 0.9) onto the sample. After reflection from the sample, the light is recollected by the objective lens and steered to the camera by the non-polarizing beam splitter (NBS). A CMOS camera (Thorlabs, DCC3240C) is used to capture the images by using a second lens (L2). The sensor size is 1280x1024 and the pixel size is 5.3μm (square). Taking into account the incident wavelength and the NA, the beam size at the focus is estimated to be approximately 0.8 μm [8].

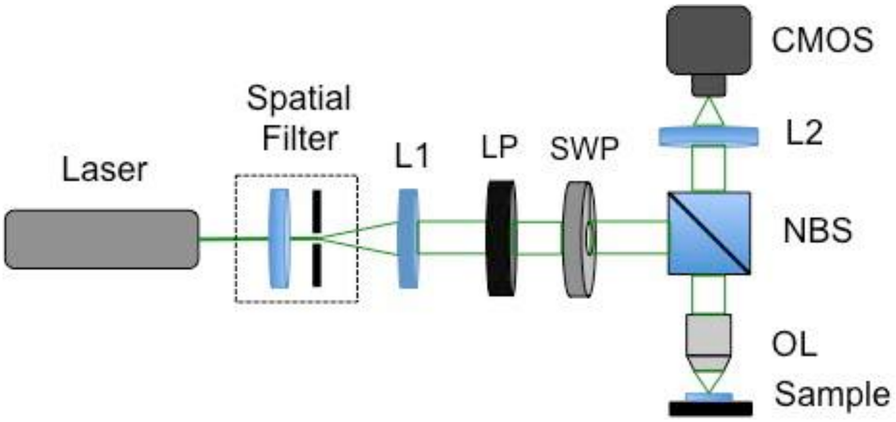

Fig. 3.11 Schematic diagram for the polarimetric experimental setup [118].

The PSG is employed to excite the sample with an x-polarization that was generated by placing a linear polarizer (LP) of the Glan-Thompson type (Thorlabs, GTH10M), without the SWP (s-wave plate) present. A linear to radial/azimuthal polarization converter (Altechna, s-wave plate, model RCP-515-06) has been employed [62, 115] to generate the radial polarization modes. This commercial device is a femtosecond laser machined nanostructure that varies spatially the phase to produce radial and azimuthal distributions of the electric field as well as polarization vortex [59]. Each sample was assembled on an *xyz* micrometric translational stage to facilitate its alignment.

Fig. 3.12 shows the experimental intensity distributions on the exit pupil plane of the objective lens when the sample is illuminated by x-linear (Fig. 3.12(a)) and radial (Fig. 3.12(b)) polarization, respectively. Observe that when the sample is illuminated with x-polarized light, after reflection, axially symmetrical dark zones appear at specific horizontal positions where the intensity takes the minimum value. Due to the electric field direction of the radially polarized is parallel to the incident local plane at each azimuthal angle of the objective lens, a dark ring could be observed, due to circular symmetry and the fact that the sample is homogeneous and isotropic (otherwise, the dark circle should not be completely closed). By the own fabrication nature of the s-wave plate, a minimum is always present at the center of the images registered by the CMOS camera.

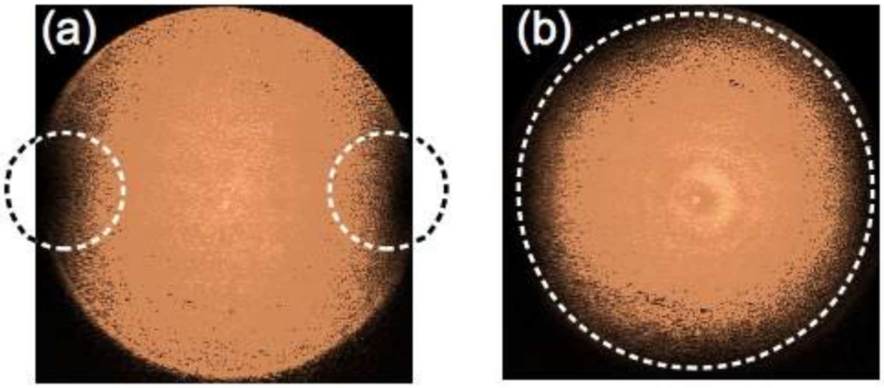

Fig. 5. Experimental intensity distributions on the exit pupil plane of the objective lens when the sample is illuminated by: (a) x-linear and (b) radial polarization. Symmetrical dark zones, highlighted by dashed lines, appear as a consequence that light is reaching the Brewster angle.

The digital procedure used to find the Brewster's angle to the experimental images is shown in the Appendix A4. It is important to mention that images present a little noise, and this could generate several minimum values, therefore the average of those values was calculated.

3.2.5 Results and discussions of the refractive index determined theoretically and experimentally.

For the Brewster angle, the experimental result (Fig. 3.12, Table III) was compared with the reported angle given by the refractive index of BK7 glass [119].

Table III. Measurement results of the Brewster angle and the refractive index of a BK7 glass by polarimetry.

Parameter	Reported value	Theoretical value	Incident polarization	
			x-polarized	Radial polarized
θ_B	56.650	56.590	56.349±1.279	56.116±1.502
n	1.519	1.516	1.504±0.071	1.492±0.082

According to the Table III, when the incident beam is x-polarized light, the results are closer to the reported value and have a smaller error than the results for the radially polarized results. The advantage of using radial polarized light is that this kind of illumination contains all linear polarizations depending on the azimuthal angle and it could be applied to test the anisotropy of sample in a single measurement. The difference between experimental and simulated results may be due to the fact that the experimental results are measured from a micro-metric region, within the focus, which is assumed to be homogeneous and isotropic; while the reported reference value is the average value obtained using a well manufactured sample and larger illuminating areas of several square mm.

Chapter 4 Conclusions

4.1 Conclusions of the polarization properties of light scattered by a metallic cylinder

In summary, the experimental determination of the Mueller's matrix (MM) associated to the light scattered from a metallic cylinder has been presented herein. Results show that this Mueller matrix has the same form as those reported for the one-dimensional rough surfaces. A very important difference between a one-dimensional rough surface that scatters light around a complete circle and a metallic cylinder, is that the rough surface depolarizes angularly while the metallic cylinder does not. With the determination of the MM, useful information about polarimetric properties of the metallic cylinder can be obtained. The depolarization index and the Gil-Bernabeu theorem have shown that the light scattered by the metallic cylinder is not depolarized, within the experimental error of the system employed here, and therefore it could be described by the Jones formalism. As a consequence of the angular dependence of the scattering, the metallic cylinder surface can be tailored properly to handle the distribution of light and its polarization properties. Several useful devices could be constructed based on this easily controllable and accessible low-cost method. For example, one possible application of the scattering behavior by a metallic circular cylinder is to use it as a polarization-maintaining de-multiplexer in combination with the plastic optical fibers (POF). The POFs are easy to handle, flexible, and economical, so the applications with POFs have been developed and commercialized, from their use as a simple light transmission guide to their utilization as sensors [120]. The scattered light by the metallic cylinder can be distributed through the optical fibers, maintaining the same polarization of incident light in each output channels for the cases of parallel and perpendicular polarizations, respectively.

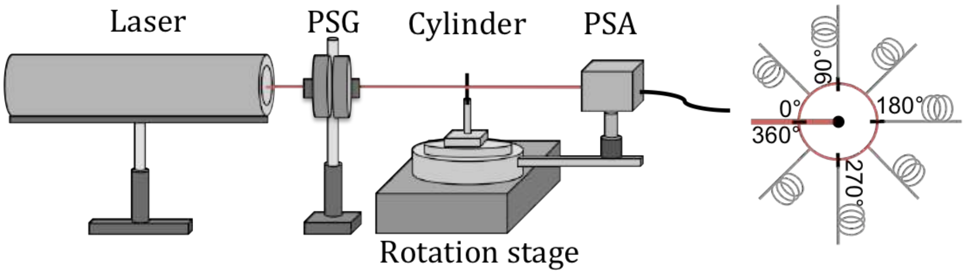

Fig. 4.1 A possible application associated to the use of plastic optical fibers acting like a polarization de-multiplexer.

For a general incident polarization state, the knowledge of the Mueller's matrix allows handling properly the desired polarization state, depending on the angular scattering position at which each single fiber is fixed (see Fig. 4.1). For instance, considering a circle with 12 cm radius (ignoring the sections on the circle where the incidence and the saturation are angularly located), it is possible to place up 30 output channels, separated 2 cm one of the other. To our knowledge, this is the cheapest and easiest controllable way to generate linear horizontal and vertical polarizations scattered fully angularly and uniformly.

4.2 Conclusions of the refractive index measurement

In summary, we have demonstrated an imaging polarimeter that measures the refractive index of a BK7 glass in a single shot. The sample was illuminated with two different polarization states, x- linear and radial polarization. Although the measured refractive index is closer to the reported value when the incident beam is x-linearly polarized, but the radial polarization also presents a good approximation. The purpose of this work is to show the importance and the application of the unconventional polarization to measure the refractive index of a dielectric sample. Probably the small error presented between the experimental and the reported values is originated from the fact that the experimental results have been obtained from illuminated regions at the micro-scale region, while the reported value considers larger areas around several square mm. The technique reported in this work allows ellipsometric measurement within the focal region, which may find applications in the microelectronic industry. This method and our numerical model can be used to generate high spatial-resolution refractive index maps when the samples under study are non-homogeneous and non-isotropic.

Future work

In the case of the light scattered by a metallic cylinder, the dependence of the polarization properties by varying the incident wavelength, the diameter and material of the cylinder can be studied.

Taking advantage of the characteristic of the radially polarized beam, a sample can be studied to determine if the sample is an isotropic or anisotropic material, also its refractive indexes can be determined in a single shot using the polarimeter. On the other hand, the source light used in the polarimeter arrangement can be changed by a monochromatic source with the aim to characterize the sample in function of the wavelength. Also, the refractive index mapping of the entire surface of a micro-structure elaborated by photolithography can be obtained, each measurement should be taken displacing the sample in fractions of micrometers depending on the resolution of the translation stage. It is possible to develop an automatic system to control the movement of the sample through step motors and simultaneously to apply a software that plots the refractive index measured.

References

1. R. A. Chipman, “Polarimetry,” chapter 22 in *Handbook of Optics II*, 2nd edition, McGraw-Hill, New York, 22.1-22.37 (1995).
2. M. Losurdo and K. Hingerl, *Ellipsometry at the Nanoscale*, Springer, Berlin (2013).
3. N. Ghosh, J. Soni, M. F. G. Wood, M. A. Wallenberg, and I. A. Vitkin, “Mueller matrix polarimetry for the characterization of complex random medium like biological tissues,” Pramana – Journal of Physics **75**(6), 1071-1086 (2010).
4. S. N. Savenkov, “Mueller Matrix Polarimetry in Material Science, Biomedical and Environmental Applications,” chapter 29 in *Handbook of Coherent-Domain Optical Methods*, 2nd edition, Springer, New York, 1175-1253 (2013).
5. J. S. Tyo, D. L. Goldstein, D. B. Chenault, and J. A. Shaw, "Review of passive imaging polarimetry for remote sensing applications," Applied Optics **45**(22), 5453-5469 (2006).
6. K. M. Salas-Alcántara, R. Espinosa-Luna, I. Torres-Gómez, Y. O. Barmenkov, “Determination of the Mueller matrix of UV-inscribed long-period fiber grating,” Applied Optics **53**(2), 269-277 (2014).
7. A. Nomura, B. Javidi, S. Murata, E. Nitanai, and T. Numata, "Polarization imaging of a 3D object by use of on-axis phase-shifting digital holography," Optics Letters **32**(2), 481-483 (2007).
8. M. Born and E. Wolf, *Principles of Optics*, 7th edition, Cambridge University Press, London (1999).
9. Q. Zhan, "Cylindrical vector beams: from mathematical concepts to applications," Advances in Optics and Photonics **1**(1), 1-57 (2009).
10. E. Hecht, *Optics*, Pearson Education, 4th edition, San Francisco (2002).
11. G. R. Fowles, *Introduction to Modern Optics*, 2nd edition, Reinhart & Winston, New York (1975).
12. D. Goldstein, *Polarized Light*, 3rd edition, CRC Press, Boca Raton (2011).

13. C. Brosseau, *Fundamentals of Polarized Light: A Statistical Optics Approach*, Wiley, New York (1998).
14. E. Collett, *Field Guide to Polarization*, SPIE Field Guides, **FG05**, SPIE (2005).
15. R. M. A. Azzam, "Stokes-vector and Mueller-matrix polarimetry [Invited]," Journal of the Optical Society of America A **33**(7), 1396-1408 (2016).
16. H. C. Van der Hulst, *Light Scattering by Small Particles*, Courier Corporation, Amsterdam (1957).
17. K. A. O´Donnell and M. E. Knotts, “Polarization dependence of scattering from one-dimensional rough surfaces,” Journal of the Optical Society of America A **8**(7), 1126-1131 (1991).
18. N. C. Bruce, A. J. Sant, and J. C. Dainty, “The Mueller matrix for rough surface scattering using the Kirchhoff approximation,” Optics Communications **88**(4-6)**,** 471-487 (1992).
19. T. R. Michel, M. E. Knotts, and K. A. O´Donnell, “Stokes matrix of a one-dimensional perfectly conducting rough surface,” Journal of the Optical Society of America A **9**(4), 585-596 (1992).
20. M. E. Knotts, T. R. Michel, and K. A. O´Donnell, “Comparisons of theory and experiment in light scattering from a randomly rough surface,” Journal of the Optical Society of America A **10**(5), 928-941 (1993).
21. G. Atondo-Rubio, R. Espinosa-Luna, and A. Mendoza-Suárez, “Mueller matrix determination for one-dimensional rough surfaces with a reduced number of measurements,” Optics Communications **244**(1), 7-13 (2005).
22. R. Espinosa-Luna, G. Atondo-Rubio, A. Mendoza-Suárez, “Complete determination of the Mueller matrix for one-dimensional rough metallic surfaces,” Optics Communications **257**(1), 62-71 (2006).
23. Rafael Espinosa-Luna, "Degree of polarization as a criterion to obtain the nine bilinear constraints between the Mueller-Jones matrix elements," Applied Optics **46**(24), 6047-6054 (2007)
24. C. Bohren and D. Huffman, *Absorption and scattering of light by small particles,* Wiley, New York (2008).
25. P. M. A. Sloot, A. G. Hoekstra, H. van der Liet, and C. G. Figdor, "Scattering matrix elements of biological particles measured in a flow through system: theory and practice," Applied Optics **28**(10), 1752-1762 (1989).

26. X. Chen, C. Zhang, and S. Liu, “Depolarization effects from nanoimprinted grating structures as measured by Mueller matrix polarimetry,” Applied Physics Letters **103**(15), 151605 (2013).
27. E. Garcia-Caurel, A. De Martino, and B. Drevillon, “Spectroscopic Mueller polarimeter based on liquid crystal devices,” Thin Solid Films **455**, 120-123 (2004).
28. J. Gil and E. Bernabeu, “Depolarization and polarization indeces of an optical system”, Journal of Modern Optics **33**(2), 185–189 (1986).
29. S. Y. Lu and R.A. Chipman, “Mueller matrices and the degree of polarization,” Optics Communications **146**(1), 11–14 (1998).
30. R. Espinosa-Luna and E. Bernabeu, “On the Q(M) depolarization metric,” Optics Communications **277**(2), 256 –258 (2007).
31. S. Savenkov, “Polarimetry in terrestrial applications,” chapter 3 in *Light scattering Reviews 10*, 85-162, Springer, Berlin (2016).
32. J. J. Gil and R. Ossikovski, *Polarized light and the Mueller matrix approach*, CRC Press (2016).
33. R. Espinosa-Luna, G. Atondo-Rubio, and O. J. Velarde-Escobar, “Métrica de despolarización escalar Q (M) como criterio para identificar sistemas retardadores o desfasadores puros,” Revista Mexicana de Fisica **56**(5), 406–410 (2010).
34. J. J. Gil and E. Bernabeu, “A depolarization criterion in Mueller matrices,” Journal of Modern Optics **32**(3), 259–261 (1985).
35. R. C. Jones, "A New Calculus for the Treatment of Optical Systems I. Description and Discussion of the Calculus," Journal of the Optics Society of America **31**(7), 488-493 (1941).
36. T. G. Brown and Q. Zhan, "Focus Issue: Unconventional Polarization States of Light," Optics Express **18**, 10775-10776 (2010).
37. T.G. Brown, “Unconventional Polarization States: Beam Propagation, Focusing, and Imaging”, *Progress in Optics* **56**, 81-129 (2011).
38. D. G. Hall, "Vector-beam solutions of Maxwell’s wave equation," Optics Letters **21**(1), 9-11 (1996).
39. K. S. Youngworth and T. G Brown, "Focusing of high numerical aperture cylindrical-vector beams," Optics Express **7**(2), 77-87 (2000).
40. A. Forbes, *Laser beam propagation*, CRC Press (2014).
41. Q. Zhan, *Vectorial optical fields*, World scientific (2014).

42. B. E. A. Saleh, and M. C. Teich, *Fundamentals of Photonics*, Wiley, New York (2007).
43. L. Novotny, and B. Hecht, *Principles of Nano-Optics,* 2nd edition, Cambridge U. Press, New York (2006).
44. D. Pohl, "Operation of a Ruby laser in the purely transverse electric mode TE_{01}," Applied Physics Letters **20**(7), 266–267 (1972).
45. K. Yonezawa, Y. Kozawa, and S. Sato, "Generation of a radially polarized laser beam by use of the birefringence of a c-cut $Nd:YV_{O4}$ crystal," Optics Letters **31**(4), 2151–2153 (2006).
46. G. Machavariani, Y. Lumer, I. Moshe, A. Meir, S. Jackel, and N. Davidson, "Birefringence-induced bifocusing for selection of radially or azimuthally polarized laser modes," Applied Optics **46**(16), 3304–3310 (2007).
47. Y. Kozawa and S.Sato, "Generation of a radially polarized laser beam by use of a conical Brewster prism," Optics Letters **30**(22), 3063–3065 (2005).
48. V. G. Niziev, R. S. Chang, and A. V. Nesterov, "Generation of inhomogeneously polarized laser beams by use of a Sagnac interferometer," Applied Optics **45**(33), 8393–8399 (2006).
49. Q. Zhan and J. R. Leger, "Microellipsometer with radial symmetry," Applied Optics **41**(22), 4630–4637 (2002).
50. Q. Zhan and J. R. Leger, "Interferometric measurement of geometric phase in space-variant polarization manipulations," Optics Communications **213**(4), 241–245 (2002).
51. G. Machavariani, Y. Lumer, I. Moshe, A. Meir, and S. Jackel, "Spatially-variable retardation plate for efficient generation of radially- and azimuthally-polarized beams," Optics Communications **281**(4), 732–738 (2008).
52. Z. Bomzon, G. Biener, V. Kleiner, and E. Hasman, "Radially and azimuthally polarized beams generated by space-variant dielectric subwavelength gratings," Optics Letters **27**(5), 285–287 (2002).
53. M. Stalder and M. Schadt, "Linearly polarized light with axial symmetry generated by liquid-crystal polarization converters," Optics Letters **21**(23), 1948–1950 (1996).
54. M. R. Beversluis, L. Novotny, and S. J. Stranick, "Programmable vector point-spread function engineering," Optics Express **14**(7), 2650–2656 (2006).
55. S. C. Tidwell, D. H. Ford, and W. D. Kimura, "Generating radially polarized beams interferometrically," Applied Optics **29**(15), 2234–2239 (1990).

56. I. Saucedo-Orozco, G. López-Morales, and R. Espinosa-Luna, "Generation of unconventional polarization from light scattered by metallic cylinders under conical incidence," Optics Letters **39**(18), 5341-5344 (2014).
57. The Z-Pol from Nanophoton (http://www.nanophoton.jp/) and the radial polarizer from ARCoptix (http://www.arcoptix.com/).
58. S-wave plate, radial polarization converter from Altechna (http://www.altechna.com).
59. M. Beresna, M. Gecevičius, P. G. Kazansky, and T. Gertus, "Radially polarized optical vortex converter created by femtosecond laser nanostructuring of glass," Applied Physics Letters **98** (20), 201101 (2011).
60. Y. Shimotsuma, P.G. Kazansky, J. Qiu, K. Hirao, "Self-Organized Nanogratings in Glass Irradiated by Ultrashort Light Pulses," Physical Review Letters **91**(24), 247405 (2003).
61. M. Beresna, M. Gecevičius, and P. G. Kazansky, "Polarization sensitive elements fabricated by femtosecond laser nanostructuring of glass [Invited]," Optical Materials Express **1**(4), 783-795 (2011).
62. Operation manual of the S-wave plate. http://www.altechna.com/download/wop/Operation-Manual-_130701.pdf
63. Azzam, R. M. A., "The intertwined history of polarimetry and ellipsometry," Thin Solid Films **519**(9), 2584-2588 (2011).
64. R. M. Azzam and N. M. Bashara, *Ellipsometry and Polarized Light*, North-Holland Pub. Co. (1977).
65. S. Y. Berezhna, I. V. Berezhnyi, O. M. Krupychm, and O. G. Vlokh, "Application of polarimetry in optical computerized tomography of anisotropic media," in proceedings of *Polarimetry and Ellipsometry*, International Society for Optics and Photonics, 169-174 (1997).
66. H. G. Tompkins, E. A. Irene, "*Handbook of ellipsometry*," Springer, New York (2005).
67. E. H. Korte and A. Röseler, "Infrared spectroscopic ellipsometry: a tool for characterizing nanometer layers," Analyst **123**(4), 647–651 (1998).
68. H. Fujiwara, *Spectroscopic Ellipsometry: Principles and Applications*, Wiley, Japan (2007).
69. H. Bloeß, J. W. Schultze, A. Michaelis, O. Genz, U. Mantz, and G. Ballantyne, "Spectroscopic anisotropy micro-ellipsometry for determination of lateral dimensions of form birefringent structures," Thin solid films, **414**(2), 246-250 (2002).

70. W. H. Weedon, S. W. McKnight, and A. J. Devaney, "Selection of optimal angles for inversion of multiple-angle ellipsometry and reflectometry equations," Journal of the Optics Society of America A **8**(12), 1881-1891 (1991).
71. T. E. Jenkins, "Multiple-angle-of-incidence ellipsometry", Journal of Physics D: Applied Physincs **32**(9), R45–R56 (1999).
72. G. H. Bu-Abbud, M. N. Bashara and J. A. Woollam, "Variable wavelength, variable angle ellipsometry including a sensitivities correlation test," Thin Solid Films **138**(1), 27–41 (1986).
73. R. M. A. Azzam, "Ellipsometry" chapter 27 in *Handbook of optical metrology*, CRC Press (2009).
74. M. Losurdo, M. Bergmair, G. Bruno, et al., "Spectroscopic ellipsometry and polarimetry for materials and systems analysis at the nanometer scale: state-of-the-art, potential, and perspectives," Journal of Nanoparticle Research **11**(7), 1521-1554 (2009).
75. Q. Zhan and J. R. Leger, "Microellipsometer with radial symmetry," Applied Optics, **41**(22), 4630-4637 (2002).
76. Q. Zhan and J. R. Leger, "High-resolution imaging ellipsometer," Applied Optics, **41**(22), 4443-4450 (2002).
77. C. Fallet, T. Novikova, M. Foldyna,S. Manhas, B. H. Ibrahim, A. A. De Martino, C. Vannuffel, and C. Constancias, "Overlay measurements by Mueller polarimetry in back focal plane," Journal of Micro/Nanolithography, MEMS, and MOEMS, **10**(3), 033017-033017 (2011).
78. S. Liu, W. Du, X. Chen, H. Jiang, and C. Zhang, "Mueller matrix imaging ellipsometry for nanostructure metrology," Optics Express **23**(13), 17316-17329 (2015).
79. B. H. Ibrahim, S. B. Hatit, and A. De Martino, "Angle resolved Mueller polarimetry with a high numerical aperture and characterization of transparent biaxial samples," Applied optics **48**(27), 5025-5034 (2009).
80. W. Khunrattanasiri and S. Boonsang, "An interferometric back focal plane microellipsometry for the determination of optical properties of a slider's air bearing surface," Signal and Information Processing Association Annual Summit and Conference (APSIPA), IEEE, 1-4 (2014).

81. Alain Tschimwang and Qiwen Zhan, "High-spatial-resolution nulling microellipsometer using rotational polarization symmetry," Applied Optics **49**(9), 1574-1580 (2010).
82. G. D. Feke, D. P. Snow, R. D. Grober, P. J. de Groot, and L. Deck, "Interferometric back focal plane microellipsometry," Applied Optics **37**(10), 1796-1802 (1998).
83. https://www.jawoollam.com/products/vase-ellipsometer.
84. H. K. Pak, B. M. Law, “2D imaging ellipsometric microscope”, Review of Scientific Instruments **66**(10), 4972-4976 (1995).
85. G. Jin, R. Jansson, and H. Arwin, “Imaging ellipsometry revisited: Developments for visualization of thin transparent layers on silicon substrates”, Review of Scientific Instruments **67**(8), 2930–2936 (1996).
86. F. Kuik, J. F. de Haan, and J. W. Hovenier, "Single scattering of light by circular cylinders," Applied Optics **33**(21), 4906-4918 (1994).
87. M. Nieto-Vesperinas and **J**.M. Soto-Crespo, “Monte Carlo simulations for scattering of electromagnetic waves from perfectly conductive random rough surfaces”, Optics Letters **12**(12), 979-981 (1987).
88. M. J. Kim, J. C. Dainty, A. T. Friberg, and A. J. Sant, “Experimental study of enhanced backscattering from one- and two-dimensional random rough surfaces”, Journal of the Optics Society of America A **7**(4), 569-577 (1990).
89. E. R. Méndez, M. A. Ponce, V. Ruiz-Cortés, and Z. H. Gu, “Photofabrication of one-dimensional rough surfaces for light-scattering experiments”, Applied Optics **30**(28), 4103-4112 (1991).
90. Y. Kuga, C. T. C. Ce, A. Ishimaru, L. Ailes-Sengers, “Analytical, experimental, and numerical studies of angular memory signatures of waves scattered from one-dimensional rough surfaces”, IEEE Transactions on Geoscience and Remote Sensing **34**(6), 1300-1307 (1996).
91. F. J. García-Vidal and L. Martín-Moreno, “Transmission and focussing of light in one-dimensional periodically nanostructured metals”, Physical Review B **66**(15), 155412 (1-10) (2002).
92. D. Felbacq, G. Tayeb, and D. Maystre, “Scattering by a random set of parallel cylinders”, Journal of the Optics Society of America A **11**(9), 2526- 2538 (1994).

93. G. Sonnichsen, T. Franzl, T. Wilk, G. von Plessen, and J. Feldmann, “Drastic reduction of plasmon damping in gold nanorods”, Physical Review Letters **88**(7), 077402 (2002).
94. A. Kienle, F. K. Forster, and R. Hibst, “Anisotropy of light propagation in biological tissue”, Optics Letters **29**(22), 2617- 2619 (2004).
95. C. J. Murphy, A. M. Gole, S. E. Hunyadi, and C. J. Orendorff, “One-dimensional coloidal gold and silver nanostructures”, Inorganic Chemestry **45**(19), 7544-7554 (2006).
96. S. C. Lee, “Light scattering by a coated infinite cylinder in an absorbing medium”, Journal of the Optics Society of America A **28**(6), 1067-1075 (2011).
97. F. Frezza, L. Pajewski, C. Ponti, G. Schettini, and N. Tedeschi, “Electromagnetic scattering by a metallic cylinder buried in a lossy medium with the cylindrical-wave approach”, IEEE Geoscience and Remote Sensing Letters **10**(1), 179- 183 (2013).
98. L. M. Sanchez-Brea, P. Siegmann, M. A. Rebollo, E. Bernabeu, “Optical technique for the automatic detection and measurement of surface defects on thin metallic wires”, Applied Optics **39**(4)**,** 539–545 (2000).
99. E. Bernabeu, I. Serroukh, L. M. Sanchez-Brea, “Geometrical model for wire optical diffraction selected by experimental statistical analysis”, Optical Engineering **38**(8), 1319-1325 (1999).
100. Gorden Videen and William S. Bickel, "Light-scattering Mueller matrix for a rough fiber," Applied Optics **31**(18), 3488-3492 (1992).
101. Gorden Videen and Dat Ngo, "Light scattering from a cylinder near a plane interface: theory and comparison with experimental data," Journal of the Optics Society of America A **14**(1), 70-78 (1997).
102. E. D. Palik, *Handbook of Optical Constants of Solids*, Academic (1985).
103. Guadalupe Lopez-Morales, Izcoatl Saucedo-Orozco, Rafael Espinosa-Luna, Qiwen Zhan, Francisco Villa-Villa, “Polarization properties of light scattered by a metallic cylinder,” (Manuscript in revision) Revista Mexicana de Física (2017).
104. K. M. Salas-Alcántara, R. Espinosa-Luna, I. Torres-Gómez, “Polarimetric Mueller-Stokes analysis of photonic crystal fibers with mechanically induced long-period gratings”, Opt. Eng. **51**(8), 085005(1-8) (2012).
105. C. W. See, M. G. Somekh, and R. D. Holmes, “Scanning optical microellipsometry for pure surface profiling,” Applied Optics **35**(34), 6663–6668 (1996).

106. S. Ye, S. H. Kim, Y. K. Kwak, H. M. Cho, Y. J. Cho, and W. Chegal, “Angle-resolved annular data acquisition method for microellipsometry,” Optics Express **15**(26), 18056–18065 (2007).

107. Q. H. Wu and I. Hodgkinson, "Precision of Brewster-angle methods for optical thin films", Journal of the Optics Society of America A **10**(9), 2072-2075 (1993).

108. C. Bahrim and Wei-Tai Hsu, “Precise measurements of the refractive indices for dielectrics using and improved Brewster angle method,” American Journal of Physics **77**(4), 337-343 (2009).

109. T. Kihara and K. Yokomori, "Simultaneous measurement of the refractive index and thickness of thin films by S-polarized reflectances", Applied Optics **31**(22), 4482-4487 (1992).

110. R. Ulrich and R. Torge, "Measurement of thin film parameters with a prism coupler", Applied Optics **12**(12), 2901-2908 (1973).

111. S. Singh, “Refractive index measurement and its applications”, Physica Scripta **65**(2), 167-180 (2002).

112. A. J. Werner, "Methods in high precision refractometry of optical glasses", Applied Optics **7**(5), 837-843 (1968).

113. S. Kim, J. Na, M. J. Kim, and B. H. Lee, "Simultaneous measurement of refractive index and thickness by combining low-coherence interferometry and confocal optics", Optics Express **16**(8), 5516-5526 (2008).

114. S. C. Zilio, "Simultaneous thickness and group index measurement with a single arm low-coherence interferometer", Optics Express **22**(22), 27392-27397 (2014).

115. Y. Kim, K. Hibino, N. Sugita, and M. Mitsuishi, "Absolute optical thickness measurement of transparent plate using excess fraction method and wavelength-tuning Fizeau interferometer", Optics Express **23**(4), 4065-4073 (2015).

116. R. Espinosa-Luna, G. López-Morales, V. M. Rico-Botero, and E. Aguilar-Fernández, “Spatial average symmetry associated to unconventional polarization,” Rev. Mex. Fis. **63**(2), 205-210 (2017).

117. As a matter of fact, an experimental evaluation revealed that it is necessary to rotate an angle of 45° between the alignment mark and the incident linear polarization to obtain the right mode. We have tested for the model RCP-515-06 (two S-waveplates).

118. Guadalupe Lopez-Morales, Victor-Manuel Rico-Botero, Rafael Espinosa-Luna, and Qiwen Zhan, “Refractive index measurement of dielectric samples using highly

focused radial polarized light (Invited Paper)," Chinese Optics Letters **15**(3), 030004 (2017).

119. Schott Inc., “Optical glass datasheet”, http://www.us.schott.com/advanced_optics/english/download/schott-optical-glass-collection-datasheets-july-2015-us.pdf.
120. J. Zubia and J. Arrue, “Plastic optical fibers: An introduction to their technological processes and applications,” Optical Fiber Technology **7**(2), 101-104 (2001).

Appendix A1

The polarization state analyzer (PSA) used to obtain the angularly resolved Stokes vector is a commercially available head (Thorlabs, model PAX5710/VIS). The data are saved in a file with extension CSV.

MATLAB code to determine the angularly resolved Mueller matrix and polarimetric parameters associated to the scattered light by a metallic cylinder.

```
% MATLAB code to determine the angularly resolved Mueller matrix and
% polarimetric parameters associated to the scattered light
% by a metallic cylinder.

% StokesVector is a function that return the Stokes vector.
% i = p(parallel) ,s (perpendicular),x (+45),y (-45),r (circular
% right),and l (circular left) polarization states.
% poweri = incident power values = S0
% S1 is Stokes parameter S1
% S2 is Stokes parameter S2
% S3 is Stokes parameter S3
% t is the capture time
% DoP is the degree of polarization.

clear all; close all; clc;

% References data taken off the air Stokes vector
% The Stokes vector of the scattered light by the air.
ref = csvread('pr.csv',24,0); % Load the data p incident polarization
[powerp,s1,s2,s3,t,DoP] = StokesVector(ref); % p - Stokes vector
ref = csvread('sr.csv',24,0); % Load the data s incident polarization
[powers,s1,s2,s3,t,DoP] = StokesVector(ref); % s - Stokes vector
ref = csvread('xr.csv',24,0); % Load the data x incident polarization
[powerx,s1,s2,s3,t,DoP] = StokesVector(ref); % x - Stokes vector
ref = csvread('yr.csv',24,0); % Load the data y incident polarization
[powery,s1,s2,s3,t,DoP] = StokesVector(ref); % y - Stokes vector
ref = csvread('rr.csv',24,0); % Load the data r incident polarization
[powerr,s1,s2,s3,t,DoP] = StokesVector(ref); % r - Stokes vector
ref = csvread('lr.csv',24,0); % Load the data l incident polarization
[powerl,s1,s2,s3,t,DoP] = StokesVector(ref);% l - Stokes vector

% Stokes vector (SV) for the scattered light by a metallic cylinder.
```

```
% -------------------- P incident polarization --------------------
pp = csvread('p.csv',24,0); % Load the data p incident polarization
[power,s1,s2,s3,t,DoP] = StokesVector(pp); % p - Stokes vector
s0 = power./powerp; % Calculation of the normalized Stokes vector respect
% to the reference power.
DoP = DoP/100; % Degree of polarization (0-1)
Gr = 0:360/(1024-1):360; % Azimuthal angles (0-360 degrees)
p = horzcat(Gr',s0,s1,s2,s3,DoP); % Stokes vector for p-incident
polarization

% -------------------- S incident polarization--------------------
pp = csvread('s.csv',24,0); % Load the data s incident polarization
[power,s1,s2,s3,t,DoP] = StokesVector(pp); % s - Stokes vector
s0 = power./powers;
DoP = DoP/100;
s = horzcat(Gr',s0,s1,s2,s3,DoP); % Stokes vector for s-incident
polarization

% -------------------- X incident polarization --------------------
pp = csvread('x.csv',24,0); % Load the data x incident polarization
[power,s1,s2,s3,t,DoP] = StokesVector(pp); % x - Stokes vector
s0 = power./powerx;
DoP = DoP/100;
x = horzcat(Gr',s0,s1,s2,s3,DoP); % Stokes vector for x-incident
polarization

% -------------------- Y incident polarization --------------------
pp = csvread('y.csv',24,0); % Load the data y incident polarization
[power,s1,s2,s3,t,DoP] = StokesVector(pp); % y - Stokes vector
s0 = power./powery;
DoP = DoP/100;
y = horzcat(Gr',s0,s1,s2,s3,DoP);% Stokes vector for y-incident
polarization

% -------------------- R incident polarization --------------------
pp = csvread('r.csv',24,0); % Load the data r incident polarization
[power,s1,s2,s3,t,DoP] = StokesVector(pp); % r - Stokes vector
s0 = power./powerr;
DoP = DoP/100;
r = horzcat(Gr',s0,s1,s2,s3,DoP); % Stokes vector for r-incident
polarization

% -------------------- L incident polarization --------------------
pp = csvread('l.csv',24,0); % Load the data l incident polarization
[power,s1,s2,s3,t,DoP] = StokesVector(pp); % l - Stokes vector
s0 = power./powerl;
DoP = DoP/100;
l = horzcat(Gr',s0,s1,s2,s3,DoP);% Stokes vector for l-incident
polarization

%------------------------ Six measurements method -----------------------
-
% Experimental determination of the effective Mueller matriz (mije) in
% function of the scattered (azimuth) angles.
% i,j=0,1,2,3.
% g: variable of the numbers of scattered grades.
```

```
        for g = 1:1024
            m00e=0.5*(p(g,2)+s(g,2));
            m01e=0.5*(p(g,2)-s(g,2));
            m02e=0.5*(x(g,2)-y(g,2));
            m03e=0.5*(r(g,2)-l(g,2));
            m10e=0.5*(p(g,3)*p(g,2)*p(g,6)+s(g,3)*s(g,2)*s(g,6));
            m11e=0.5*(p(g,3)*p(g,2)*p(g,6)-s(g,3)*s(g,2)*s(g,6));
            m12e=0.5*(x(g,3)*x(g,2)*x(g,6)-y(g,3)*y(g,2)*y(g,6));
            m13e=0.5*(r(g,3)*r(g,2)*r(g,6)-l(g,3)*l(g,2)*l(g,6));

            m20e=0.5*(p(g,4)*p(g,2)*p(g,6)+s(g,4)*s(g,2)*s(g,6));
            m21e=0.5*(p(g,4)*p(g,2)*p(g,6)-s(g,4)*s(g,2)*s(g,6));
            m22e=0.5*(x(g,4)*x(g,2)*x(g,6)-y(g,4)*y(g,2)*y(g,6));
            m23e=0.5*(r(g,4)*r(g,2)*r(g,6)-l(g,4)*l(g,2)*l(g,6));

            m30e=0.5*(p(g,5)*p(g,2)*p(g,6)+s(g,5)*s(g,2)*s(g,6));
            m31e=0.5*(p(g,5)*p(g,2)*p(g,6)-s(g,5)*s(g,2)*s(g,6));
            m32e=0.5*(x(g,5)*x(g,2)*x(g,6)-y(g,5)*y(g,2)*y(g,6));
            m33e=0.5*(r(g,5)*r(g,2)*r(g,6)-l(g,5)*l(g,2)*l(g,6));

            % Experimental effective Mueller matrix, Meff.
            Meff=[m00e m01e m02e m03e; m10e m11e m12e m13e; m20e m21e
m22e m23e; m30e m31e m32e m33e];
            Meffexp(:,g) = Meff(:);

            % Normalized experimental effective Mueller matrix respect to
            % m00e value.
            mt=(1/m00e)*Meff;

            m00n(g,1) = mt(1,1);
            m01n(g,1) = mt(1,2);
            m02n(g,1) = mt(1,3);
            m03n(g,1) = mt(1,4);
            m10n(g,1) = mt(2,1);
            m11n(g,1) = mt(2,2);
            m12n(g,1) = mt(2,3);
            m13n(g,1) = mt(2,4);
            m20n(g,1) = mt(3,1);
            m21n(g,1) = mt(3,2);
            m22n(g,1) = mt(3,3);
            m23n(g,1) = mt(3,4);
            m30n(g,1) = mt(4,1);
            m31n(g,1) = mt(4,2);
            m32n(g,1) = mt(4,3);
            m33n(g,1) = mt(4,4);

% ------------------- Polarization parameter calculus -------------------

            % Depolarization index, 0<=DI(M)<=1.
            L1 = mt(1,2)^2 + mt(1,3)^2 + mt(1,4)^2 + mt(2,1)^2 +
mt(2,2)^2 + mt(2,3)^2 + mt(2,4)^2;
            L2 = mt(3,1)^2 + mt(3,2)^2 + mt(3,3)^2 + mt(3,4)^2 +
mt(4,1)^2 + mt(4,2)^2 + mt(4,3)^2 + mt(4,4)^2;
            LT = sqrt(L1 + L2);
            DI(g,1) = LT/(sqrt(3)*mt(1,1));
            % Diattenuation, 0<=D(M)<=1.
            DM(g,1) = ((mt(1,2).^2 + mt(1,3).^2 +
```

```
mt(1,4).^2).^(1/2))/mt(1,1);
            % Polarizance, 0<=P(M)<=1
            PM(g,1) = ((mt(2,1).^2 + mt(3,1).^2 +
mt(4,1).^2).^(1/2))/mt(1,1);
            % Gil-Bernabeu Theorem
            MT=trace(mt*mt');
            ME=4*(mt(1,1)^2);
            TC(g,1) = MT/ME;

%             Deleting data around 180 degrees due to the saturation on
the detector.

            if g > 1007 || g < 16 || (g > 490 & g < 542)
                DI(g,1) = NaN;
                DM(g,1) = NaN;
                DL(g,1) = NaN;
                DC(g,1) = NaN;
                PM(g,1) = NaN;
                QM(g,1) = NaN;
                TC(g,1) = NaN;

                m00n(g,1) = NaN;
                m01n(g,1) = NaN;
                m02n(g,1) = NaN;
                m03n(g,1) = NaN;
                m10n(g,1) = NaN;
                m11n(g,1) = NaN;
                m12n(g,1) = NaN;
                m13n(g,1) = NaN;
                m20n(g,1) = NaN;
                m21n(g,1) = NaN;
                m22n(g,1) = NaN;
                m23n(g,1) = NaN;
                m30n(g,1) = NaN;
                m31n(g,1) = NaN;
                m32n(g,1) = NaN;
                m33n(g,1) = NaN;

                DoP(g,1) = NaN;
            end
        end


% ------------------ Plotting Mueller matrix elements ------------------

error = 10/100;
step = 10;
limY = 1.5;
step2 = 40;
lwl = 1.5;
ft = 27;
fl = 27;
fe = 20;
lw = 1.2;

figure (1)
```

```
subplot(4,4,1); plot(Gr(1:step:1024)',m00n(1:step:1024),'LineWidth',lwl);
hold on
ylim([-limY limY]); xlim([0 360]);
ylabel('m00','fontsize',fl,'fontweight','b');
set(gca,'XTick',0:360/4:360)
set(gca,'XTickLabel',{'0','90','180','270','360'})
set(gca,'Fontsize',fe,'fontweight','b','LineWidth',lw)
grid on; legend boxoff;

subplot(4,4,2); plot(Gr(1:step:1024)',m01n(1:step:1024),'LineWidth',lwl);
hold on
ylim([-limY limY]); xlim([0 360]);
ylabel('m01','fontsize',fl,'fontweight','b');
set(gca,'XTick',0:360/4:360)
set(gca,'XTickLabel',{'0','90','180','270','360'})
set(gca,'Fontsize',fe,'fontweight','b','LineWidth',lw)
grid on; legend boxoff;

subplot(4,4,3); plot(Gr(1:step:1024)',m02n(1:step:1024),'LineWidth',lwl);
hold on
errorbar(Gr(step:step2:490)',zeros(size(Gr(step:step2:490)))',error*ones(
size(Gr(step:step2:490)))','.m','MarkerSize',1);
errorbar(Gr(560:step2:1007)',zeros(size(Gr(560:step2:1007)))',error*ones(
size(Gr(560:step2:1007)))','.m','MarkerSize',1);
ylim([-limY limY]); xlim([0 360]);
ylabel('m02','fontsize',fl,'fontweight','b');
set(gca,'XTick',0:360/4:360)
set(gca,'XTickLabel',{'0','90','180','270','360'})
set(gca,'Fontsize',fe,'fontweight','b','LineWidth',lw)
grid on; legend boxoff;

subplot(4,4,4);
plot(Gr(1:step:1024)',m03n(1:step:1024),'LineWidth',lwl);hold on
errorbar(Gr(step:step2:490)',zeros(size(Gr(step:step2:490)))',error*ones(
size(Gr(step:step2:490)))','.m','MarkerSize',1);
errorbar(Gr(560:step2:1007)',zeros(size(Gr(560:step2:1007)))',error*ones(
size(Gr(560:step2:1007)))','.m','MarkerSize',1);
ylim([-limY limY]); xlim([0 360]);
ylabel('m03','fontsize',fl,'fontweight','b');
set(gca,'XTick',0:360/4:360)
set(gca,'XTickLabel',{'0','90','180','270','360'})
set(gca,'Fontsize',fe,'fontweight','b','LineWidth',lw)
grid on; legend boxoff;

subplot(4,4,5); plot(Gr(1:step:1024)',m10n(1:step:1024),'LineWidth',lwl);
hold on
ylim([-limY limY]); xlim([0 360]);
ylabel('m10','fontsize',fl,'fontweight','b');
set(gca,'XTick',0:360/4:360)
set(gca,'XTickLabel',{'0','90','180','270','360'})
set(gca,'Fontsize',fe,'fontweight','b','LineWidth',lw)
grid on; legend boxoff;

subplot(4,4,6);
plot(Gr(1:step:1024)',m11n(1:step:1024),'LineWidth',lwl);hold on
ylim([-limY limY]); xlim([0 360]);
ylabel('m11','fontsize',fl,'fontweight','b');
```

```
set(gca,'XTick',0:360/4:360)
set(gca,'XTickLabel',{'0','90','180','270','360'})
set(gca,'Fontsize',fe,'fontweight','b','LineWidth',lw)
grid on; legend boxoff;

subplot(4,4,7); plot(Gr(1:step:1024)',m12n(1:step:1024),'LineWidth',lwl);
hold on
errorbar(Gr(step:step2:490)',zeros(size(Gr(step:step2:490)))',error*ones(
size(Gr(step:step2:490)))','.m','MarkerSize',1);
errorbar(Gr(560:step2:1007)',zeros(size(Gr(560:step2:1007)))',error*ones(
size(Gr(560:step2:1007)))','.m','MarkerSize',1);
ylim([-limY limY]); xlim([0 360]);
ylabel('m12','fontsize',fl,'fontweight','b');
set(gca,'XTick',0:360/4:360)
set(gca,'XTickLabel',{'0','90','180','270','360'})
set(gca,'Fontsize',fe,'fontweight','b','LineWidth',lw)
grid on; legend boxoff;

subplot(4,4,8); plot(Gr(1:step:1024)',m13n(1:step:1024),'LineWidth',lwl);
hold on
errorbar(Gr(step:step2:490)',zeros(size(Gr(step:step2:490)))',error*ones(
size(Gr(step:step2:490)))','.m','MarkerSize',1);
errorbar(Gr(560:step2:1007)',zeros(size(Gr(560:step2:1007)))',error*ones(
size(Gr(560:step2:1007)))','.m','MarkerSize',1);
ylim([-limY limY]); xlim([0 360]);
ylabel('m13','fontsize',fl,'fontweight','b');
set(gca,'XTick',0:360/4:360)
set(gca,'XTickLabel',{'0','90','180','270','360'})
set(gca,'Fontsize',fe,'fontweight','b','LineWidth',lw)
grid on; legend boxoff;

subplot(4,4,9); plot(Gr(1:step:1024)',m20n(1:step:1024),'LineWidth',lwl);
hold on
errorbar(Gr(step:step2:490)',zeros(size(Gr(step:step2:490)))',error*ones(
size(Gr(step:step2:490)))','.m','MarkerSize',1);
errorbar(Gr(560:step2:1007)',zeros(size(Gr(560:step2:1007)))',error*ones(
size(Gr(560:step2:1007)))','.m','MarkerSize',1);
ylim([-limY limY]); xlim([0 360]);
ylabel('m20','fontsize',fl,'fontweight','b');
set(gca,'XTick',0:360/4:360)
set(gca,'XTickLabel',{'0','90','180','270','360'})
set(gca,'Fontsize',fe,'fontweight','b','LineWidth',lw)
grid on; legend boxoff;

subplot(4,4,10);
plot(Gr(1:step:1024)',m21n(1:step:1024),'LineWidth',lwl); hold on
errorbar(Gr(step:step2:490)',zeros(size(Gr(step:step2:490)))',error*ones(
size(Gr(step:step2:490)))','.m','MarkerSize',1);
errorbar(Gr(560:step2:1007)',zeros(size(Gr(560:step2:1007)))',error*ones(
size(Gr(560:step2:1007)))','.m','MarkerSize',1);
ylim([-limY limY]); xlim([0 360]);
ylabel('m21','fontsize',fl,'fontweight','b');
set(gca,'XTick',0:360/4:360)
set(gca,'XTickLabel',{'0','90','180','270','360'})
set(gca,'Fontsize',fe,'fontweight','b','LineWidth',lw)
grid on; legend boxoff;
```

```
subplot(4,4,11);
plot(Gr(1:step:1024)',m22n(1:step:1024),'LineWidth',lwl); hold on
ylim([-limY limY]); xlim([0 360]);
ylabel('m22','fontsize',fl,'fontweight','b');
set(gca,'XTick',0:360/4:360)
set(gca,'XTickLabel',{'0','90','180','270','360'})
set(gca,'Fontsize',fe,'fontweight','b','LineWidth',lw)
grid on; legend boxoff;

subplot(4,4,12);
plot(Gr(1:step:1024)',m23n(1:step:1024),'LineWidth',lwl); hold on
ylim([-limY limY]); xlim([0 360]);
ylabel('m23','fontsize',fl,'fontweight','b');
set(gca,'XTick',0:360/4:360)
set(gca,'XTickLabel',{'0','90','180','270','360'})
set(gca,'Fontsize',fe,'fontweight','b','LineWidth',lw)
grid on; legend boxoff;

subplot(4,4,13);
plot(Gr(1:step:1024)',m30n(1:step:1024),'LineWidth',lwl); hold on
errorbar(Gr(step:step2:490)',zeros(size(Gr(step:step2:490)))',error*ones(
size(Gr(step:step2:490)))','.m','MarkerSize',1);
errorbar(Gr(560:step2:1007)',zeros(size(Gr(560:step2:1007)))',error*ones(
size(Gr(560:step2:1007)))','.m','MarkerSize',1);
ylim([-limY limY]); xlim([0 360]);
ylabel('m30','fontsize',fl,'fontweight','b');
set(gca,'XTick',0:360/4:360)
set(gca,'XTickLabel',{'0','90','180','270','360'})
set(gca,'Fontsize',fe,'fontweight','b','LineWidth',lw)
grid on; legend boxoff;

subplot(4,4,14);
plot(Gr(1:step:1024)',m31n(1:step:1024),'LineWidth',lwl); hold on
errorbar(Gr(step:step2:490)',zeros(size(Gr(step:step2:490)))',error*ones(
size(Gr(step:step2:490)))','.m','MarkerSize',1);
errorbar(Gr(560:step2:1007)',zeros(size(Gr(560:step2:1007)))',error*ones(
size(Gr(560:step2:1007)))','.m','MarkerSize',1);
ylim([-limY limY]); xlim([0 360]);
ylabel('m31','fontsize',fl,'fontweight','b');
set(gca,'XTick',0:360/4:360)
set(gca,'XTickLabel',{'0','90','180','270','360'})
set(gca,'Fontsize',fe,'fontweight','b','LineWidth',lw)
grid on; legend boxoff;

subplot(4,4,15);
plot(Gr(1:step:1024)',m32n(1:step:1024),'LineWidth',lwl); hold on
ylim([-limY limY]); xlim([0 360]);
ylabel('m32','fontsize',fl,'fontweight','b');
set(gca,'XTick',0:360/4:360)
set(gca,'XTickLabel',{'0','90','180','270','360'})
set(gca,'Fontsize',fe,'fontweight','b','LineWidth',lw)
grid on; legend boxoff;

subplot(4,4,16);
plot(Gr(1:step:1024)',m33n(1:step:1024),'LineWidth',lwl); hold on
ylim([-limY limY]); xlim([0 360]);
ylabel('m33','fontsize',fl,'fontweight','b');
```

```
set(gca,'XTick',0:360/4:360)
set(gca,'XTickLabel',{'0','90','180','270','360'})
set(gca,'Fontsize',fe,'fontweight','b','LineWidth',lw)
grid on; legend boxoff;

text(-950,-3,'Scattering Angle
(degrees)','fontsize',fl,'fontweight','b');


% ------------------- Plotting polarimetric parameters ------------------
-
error = 4/100;
step = 20;
step2 = 20;
step3 = 40;
step4 = 40;

figure (2)
plot(Gr(1:step2:1024)',DI(1:step2:1024),'-
sr',Gr(1:step:1024)',TC(1:step:1024),'-k',...
    Gr(1:step2:1024)',DM(1:step2:1024),'--
o',Gr(1:step:1024)',PM(1:step:1024),'-+','LineWidth',2);
hold on;
ylim([-0.1 1.5]); xlim([0 360]);
xlabel('Scattering Angle (degrees)','fontsize',30,'fontweight','b');
legend('Depolarization Index','Gil-Bernabeu
Theorem','Diattenuation','Polarizance');
set(gca,'XTick',0:360/8:360)
set(gca,'XTickLabel',{'0','45','90','135','180','225','270','315','360'})
set(gca,'Fontsize',25,'fontweight','b','LineWidth',2.2)
box off; grid on;
```

Function to obtain the Stokes vector to the CSV file.

```
% Function that taken off the Stokes parameters for the PAX software
function [power,s1,s2,s3,t,DoP] = StokesVector(p)
    power = p(1:1024,11); % Incident power values = S0
    a = power(1:257); b = power(258:1024);
    power = cat(1,b,a);  % Re-ordering of the power values
    s1 = p(1:1024,2); % Incident Stokes parameter, S1
    a = s1(1:257); b = s1(258:1024);
    s1 = cat(1,b,a); % Re-ordering of the S1 values
    s2 = p(1:1024,3); % Incident Stokes parameter, S2
    a = s2(1:257); b = s2(258:1024);
    s2 = cat(1,b,a); % Re-ordering of the S2 values
    s3 = p(1:1024,4); % Incident Stokes parameter, S3
    a = s3(1:257); b = s3(258:1024);
    s3 = cat(1,b,a); % Re-ordering of the S3 values
    t = p(1:1024,1); % time
%     a = t(1:257); b = t(258:1024); % Re-ordering of the t values
    DoP = p(1:1024,9); % Incident degree of polarization
    a = DoP(1:257); b = DoP(258:1024);
    DoP = cat(1,b,a); % Re-ordering of the DoP values
```

Appendix A2

Matlab code to calculate the Spatial Average Symmetry associated to radial and azimuthal polarization beam.

```
% STOKESVECTORFROMIMAGE    Calculate the Stokes vector associated to a
%                          image. The only input parameter is the image
%                          name (for example: 'IMG5423.tif'). The output
%                          parameter is the Stokes vector So=[s0..s3].
%
% By: V?ctor-Manuel Rico-Botero
% 2016-Jun-26th

clear all
clc
%% -------------------Load of experimental image-------------------------
--
SourceImage=imread('Radial.tif');
P=imread('Radial_PolP.tif');
S=imread('Radial_PolS.tif');
U=imread('Radial_Pol+45.tif');
D=imread('Radial_Pol-45.tif');
R=imread('Radial_PolCR.tif');
L=imread('Radial_PolCL.tif');
%% ----------------------Graylevel---------------------------------------
--
SourceImage=double(rgb2gray(SourceImage(:,:,1:3)));
P=rgb2gray(P(:,:,1:3));
S=rgb2gray(S(:,:,1:3));
U=rgb2gray(U(:,:,1:3));
D=rgb2gray(D(:,:,1:3));
R=rgb2gray(R(:,:,1:3));
L=rgb2gray(L(:,:,1:3));
%% ---------------cropping for unanalyzed image--------------------------
--
imagesc(SourceImage)
[x,y]=ginput;
SourceImage_cropped=imcrop(SourceImage,[x-400,y-400,800,800]);
imagesc(SourceImage_cropped/max(max(SourceImage_cropped)))
axis 'square'
colorbar
set(gca, 'fontsize', 18)
saveas(figure(1),'0_SourceImage_cropped','tif');
close all
%% ----------cropping for circular linear P analyzed image---------------
--
```

```
imagesc(P)
[x,y]=ginput;
P_cropped=double(imcrop(P,[x-400,y-400,800,800]));
imagesc(P_cropped/max(max(P_cropped)))
axis 'square'
colorbar
set(gca, 'fontsize', 18)
saveas(figure(1),'1_P_cropped','tif');
close all
%% ----------cropping for circular linear S analyzed image---------------
--
imagesc(S)
[x,y]=ginput;
S_cropped=double(imcrop(S,[x-400,y-400,800,800]));
imagesc(S_cropped/max(max(S_cropped)))
axis 'square'
colorbar
set(gca, 'fontsize', 18)
saveas(figure(1),'2_S_cropped','tif');
close all
%% ---------cropping for circular linear +45? analyzed image-------------
--
imagesc(U)
[x,y]=ginput;
U_cropped=double(imcrop(U,[x-400,y-400,800,800]));
imagesc(U_cropped/max(max(U_cropped)))
axis 'square'
colorbar
set(gca, 'fontsize', 18)
saveas(figure(1),'3_U_cropped','tif');
close all
%% ---------cropping for circular linear -45? analyzed image-------------
--
imagesc(D)
[x,y]=ginput;
D_cropped=double(imcrop(D,[x-400,y-400,800,800]));
imagesc(D_cropped/max(max(D_cropped)))
axis 'square'
colorbar
set(gca, 'fontsize', 18)
saveas(figure(1),'4_D_cropped','tif');
close all
%% ---------cropping for circular right hand analyzed image--------------
--
imagesc(R)
[x,y]=ginput;
R_cropped=double(imcrop(R,[x-400,y-400,800,800]));
imagesc(R_cropped/max(max(R_cropped)))
axis 'square'
colorbar
set(gca, 'fontsize', 18)
saveas(figure(1),'5_R_cropped','tif');
close all
%% ---------cropping for circular left hand analyzed image---------------
--
imagesc(L)
[x,y]=ginput;
L_cropped=double(imcrop(L,[x-400,y-400,800,800]));
```

```
imagesc(L_cropped/max(max(L_cropped)))
axis 'square'
colorbar
set(gca, 'fontsize', 18)
saveas(figure(1),'6_L_cropped','tif');
close all
%% --------------Calculation of pixel's distance matrices------------------
[x,y]=meshgrid(-400:400);
r=sqrt(x.^2+y.^2);
%% ------------------Stokes parameters calculation-------------------------
s0=mean(mean(P_cropped(r<400)+S_cropped(r<400)));
s1=mean(mean(P_cropped(r<400)-S_cropped(r<400)));
s2=mean(mean(U_cropped(r<400)-D_cropped(r<400)));
s3=mean(mean(R_cropped(r<400)-L_cropped(r<400)));
figure(1)
s0_image=(double(P_cropped)+double(S_cropped));
imagesc(s0_image/max(max(s0_image)))
colorbar
axis 'square'
set(gca, 'fontsize', 18)
saveas(figure(1),'s0_expRDL','tif');
figure(2)
s1_image=(double(P_cropped)-double(S_cropped));
imagesc(s1_image/max(max(s1_image)))
colorbar
axis 'square'
set(gca, 'fontsize', 18)
saveas(figure(2),'s1_expRDL','tif');
figure(3)
s2_image=(double(U_cropped)-double(D_cropped));
imagesc(s2_image/max(max(s2_image)))
colorbar
axis 'square'
set(gca, 'fontsize', 18)
saveas(figure(3),'s2_expRDL','tif');
figure(4)
s3_image=(double(R_cropped)-double(L_cropped));
imagesc(s3_image/max(max(s3_image)))
colorbar
axis 'square'
set(gca, 'fontsize', 18)
saveas(figure(4),'s3_expRDL','tif');

S=[s0 s1 s2 s3]';
Snorm=S/s0
```

Appendix A3

Theoretical analysis for measuring the refractive index to dielectric sample.

```
% Refractive index measurement of a sample illuminating with p- and
radial polarized light using a microscopic objective lens.
% by: Victor-Manuel Rico-Botero
% 2016-May-01st
% Edit by Guadalupe Lopez Morales Oct 18, 2016

%     Calculate the reflectance image for a given polarization field,
using
%     the Jones formulism.
%     E_x :    horizontal Jones component for the incident electric field
%     E_y :    vertical Jones component for the incident electric field
%     delta:   retardance between horizontal and vertical electric fields
%     polType: 'conv' for conventional polarization; 'unconv' for
%              unconventional polarization modes
%     n_s:     Average refractive index for the sample
%     NA:      Numerical aperture for the objective lens
%     tol:     tolerance arround the central refractive index value
%     diameter: diameter (in pixels) for the interest area.

clear all; clc;
close all;


% Variables
% For P incident polarization
E_x = 1;
E_y = 0;
delta = 0;
polType = 'conv';
n_s = 1.519;
NA = 0.9;
tol = 0;
diameter = 600;

% For radial incident polarization
% E_x = 1;
% E_y = 1;
% delta = 0;
% polType = 'unconv_r';
% n_s = 1.519;
```

```
% NA = 0.9;
% tol = 0;
% diameter = 600;


rho = diameter/2; % image radii
thetaMax = asin(NA); % angle (in rad) asociated to NA
f = rho/sin(thetaMax); % focal distance applying the Sine-condition
pixelsVector = -rho:rho-1;
[x,y] = meshgrid(pixelsVector); % coordinate matrix
r = sqrt(x.^2+y.^2);

%% ---------------azimthal angles for the objective lens-----------------
----
quadrantI = (x>=0)&(y>=0);
quadrantII = (x<0)&(y>=0);
quadrantIII = (x<0)&(y<0);
quadrantIV = (x>=0)&(y<0);
phyI = atan(y./x).*quadrantI;
phyII = (atan(y./x)+pi).*quadrantII;
phyIII = (atan(y./x)+pi).*quadrantIII;
phyIV = (atan(y./x)+2*pi).*quadrantIV;
phy = phyI+phyII+phyIII+phyIV;
phy(isnan(phy))=0;
%% --------------------Incident electric field---------------------------
--
switch polType
    case 'conv'
        Ex=E_x*ones(length(x),length(y))*exp(1i*delta); % Matrix for
horizontal electric field before to objective lens
        Ey=E_y*ones(length(x),length(y)); % Matrix for vertical electric
field before to objective lens
    case 'unconv_r'
        [Ex,Ey]=rAndAV2('r',532E-9,6,0,1,diameter);
    case 'unconv_a'
        [Ex,Ey]=rAndAV2('a',532E-9,6,0,1,diameter);
end
%% -------------Angle of the incident electric field---------------------
--
ExPositive = Ex>0;
ExNegative = Ex<0;
EyPositive = Ey>0;
EyNegative = Ey<0;
alphaI = atan(Ey./Ex).*ExPositive.*EyPositive;
alphaII = (atan(Ey./Ex)+pi).*ExNegative.*EyPositive;
alphaIII = (atan(Ey./Ex)+pi).*ExNegative.*EyNegative;
alphaIV = (atan(Ey./Ex)+2*pi).*ExPositive.*EyNegative;
alpha = alphaI+alphaII+alphaIII+alphaIV;
if(strcmp(polType,'unconv_r')||strcmp(polType,'unconv_a'))
    alpha=alpha';
end
if(strcmp(polType,'conv'))
    alpha=atan(Ey./Ex);  % polarization angle
end
%% ------------Magnitude of the incident electric field------------------
--
E = sqrt(Ex.*conj(Ex)+Ey.*conj(Ey));
%% -----------Incident Electric field at the plane of incidence----------
```

```
--
Ep_i = E.*cos((phy-alpha));
Es_i = sqrt((E.*cos(alpha)-Ep_i.*cos(phy)).^2+(E.*sin(alpha)-
Ep_i.*sin(phy)).^2);
%% ----------------------refractive index map----------------------------
--
theta_i = asin(r/f); % incidence angle applying the Sine-condition
n = n_s*ones(size(theta_i));  % Refractive index map. Homegeneity is
suppossed
n = n+tol*rand(size(theta_i))-tol*rand(size(theta_i));
%% ---------------Fresnel formulas for dielectrics-----------------------
--
theta_t = asin(1./n.*sin(theta_i));
r_p = (tan(theta_i-theta_t)./tan(theta_i+theta_t)); % Fresnel coefficient
for P polarization
r_s = -(sin(theta_i-theta_t)./sin(theta_i+theta_t));  % Fresnel
coefficient for S polarization
r_p(isnan(r_p)) = ((n(1)-1)/(n(1)+1)); % indeterminacy removal to normal
incidence
r_s(isnan(r_s)) = ((n(1)-1)/(n(1)+1));  % indeterminacy removal to normal
incidence
%% ------------------------Reflected fields------------------------------
--
Ep_r = r_p.*Ep_i;
Es_r = r_s.*Es_i;
%% --------------------------Reflectance---------------------------------
-
mask = r<rho;
R = sqrt((Ep_r.*conj(Ep_r)+Es_r.*conj(Es_r)).*mask);
%% ----------------------------Finding Brewster Angle--------------------
------------------
A = R;
pixelsVector = -rho:rho-1;
[x,y] = meshgrid(pixelsVector);  % position matrix
r = sqrt(x.^2+y.^2);
minValue = min(min(A(r<rho)));
intensityTolerance = 1;
idx =find(A<=minValue+intensityTolerance/1024);
[ix,iy] = ind2sub(size(A),idx);
r = sqrt((ix-rho).^2+(iy-rho).^2);
idx = idx(r<rho-2);
[ix,iy] = ind2sub(size(A),idx);
imageRadii=size(R,1)/2;
rB = sqrt((ix-imageRadii).^2+(iy-imageRadii).^2);
thetaMax = asind(NA);   % angle (in rad) asociated to NA
f = imageRadii/sind(thetaMax); % sine-condition
theoreticalBrewster_Angle = asind(mean(rB)/f)
%% Plotting
imagesc(A); axis 'square'; colormap('copper'); axis off
```

The function called RANDAV2 generates the electric field for radial or azimuthal polarization.

```
% RANDAV2  generates radial and azimuthal polarization matrices.
%          by, Victor-Manuel Rico-Botero, 2016-Apr-28th
%          Parameters:
```

```
%           polType: 'r' for radial, 'a' for azimuthal
%           lambda: wavelenght
%           w0: width of the beam weist
%           z: beam position at the propagation axis
%           E0: field amplitud
%           Diameter: image diameter in pixels
%    example: [Ex,Ey]=rAndAV2('r',632E-9,6,0,1.6,600)

function [Ex,Ey]=rAndAV2(polType,lambda,w0,z,E0,diameter)
rho=diameter/2;
pixelsVector=linspace(-1,1,2*rho);
[x,y]=meshgrid(pixelsVector*2E7*lambda);
% beyond to 0.001 computer dies!
k=2*pi/lambda;
% Wavevector
z0=(k*w0^2)/2;
% Rayleight length
wz=w0*sqrt(1+(z/z0)^2);
% Beam w
Rz=z*(1+(z0/z)^2);
% Radii of wavefront.
Rz(isnan(Rz))=1E10;
% NaN removal for z=0
qz=z+1i*z0;
% complex beam parameter
m=0;
n=1;
phy=(1+m+n)*atan(z/z0);
% Gouy phase
h0=1;
% Hermite polynomial h0
h1_y=2*sqrt(2)*y/wz;
% Hermite polynomial h1(y)
h1_x=2*sqrt(2)*x/wz;
% Hermite polynomial h1(x)
% -------------------------Modes calculation-----------------------------
--
E01=E0*w0/wz*h1_y.*exp(-1i*phy).*exp(-(x.^2+y.^2)*k/(2*qz));
E10=E0*w0/wz*h1_x.*exp(-1i*phy).*exp(-(x.^2+y.^2)*k/(2*qz));

switch polType
    case 'r'
        Ex=E01;
        Ey=E10;
    case 'a'
        Ex=-E10;
        Ey=E01;
end
```

Appendix A4

Experimental analysis for measuring the refractive index to dielectric sample.

```
% Refractive index measurement of a sample illuminating with p- and
radial
% polarized light using a microscopic objective lens (Experimental
results).
% by: Victor-Manuel Rico-Botero
% 2016-May-01st
% Edit by Guadalupe Lopez Morales Oct 18, 2016

clear all; clc;
close all;

% Load experimental images
Image = imread('BK7_P_TE5_FDN2_Seno.png');
% Image = imread('BK7_rad_TE5_FDN2_Seno.png');

Image = Image(:,:,1:3);
Image = rgb2gray(Image);
imagesc(Image); axis 'square'; colormap('copper'); axis off
Image = imresize(Image, [206 206]);

% ---------------------------- Input data ----------------------------
NA = 0.9; % Numerical aperture of the objective lens
epsilon = 3; % epsilon: tolerance in the absolute minimum value
imageDiameter = size(Image,1);
maxExpImage=max(max(Image));
% ---------------------Finding minimum value----------------------------
rho=imageDiameter/2;
pixelsVector=linspace(-rho,rho,imageDiameter);
[x,y]=meshgrid(pixelsVector);  % position matrix
r=sqrt(x.^2+y.^2);
tolerance = 6;
minValue=min(min(Image(r<(rho-tolerance)))); % calculation of the
absolute minimum
lowerLimit=(r<rho-tolerance)& Image>=minValue;
upperLimit=(r<rho-tolerance)& Image<(minValue+epsilon);
idx=find(lowerLimit & upperLimit);
% ----------------Calculation of the minimum position--------------------
-
[ix,iy]=ind2sub(size(Image),idx);
hold on
```

```
plot(iy,ix,'wx','linewidth',2)
hold off
% --------------------- Calculating the Brewster angle --------------------
-
R = size(Image,1)/2;
center = size(Image);
thetaMax=asin(NA); % angle (in rad) asociated to NA
f=R/sin(thetaMax);
r=sqrt((ix-center(2)/2).^2+(iy-center(1)/2).^2);
theta_Brewster=asind(r/f);
Brewster_Angle=mean(theta_Brewster);
nValue=mean(tand(theta_Brewster));
```